An *in vitro* neurogenetics platform for precision disease modeling in the mouse

Short title: Diversity Genetics in Disease Modeling

Daniel E. Cortes, Mélanie Escudero, , Austin C. Korgan, Alyssa Edwards, Selcan C. Aydin, Steven C. Munger, Kevin Charland, Zhong-Wei Zhang, Kristen M.S. O'Connell, Laura G. Reinholdt, and Martin F. Pera*

The Jackson Laboratory Bar Harbor ME 04660 USA

*Author for correspondence martin.pera@jax.org

Abstract

The power and scope of disease modeling can be markedly enhanced through the incorporation of broad genetic diversity. In the the mouse, the introduction of pathogenic mutations into a single inbred strain sometimes fails to mimic human disease. We describe a cross-species precision disease modeling platform that exploits mouse genetic diversity to bridge cell-based modeling with whole organism analysis. We developed a universal protocol that permitted robust and reproducible neural differentiation of genetically diverse human and mouse pluripotent stem cell lines, then carried out a proof of concept study of the neurodevelopmental gene *DYRK1A*. The results *in vitro* reliably predicted the effects of genetic background on *DYRK1A* loss of function phenotypes and identified optimal mouse strains for *in vivo* disease modeling. Transcriptomic comparison of responsive and unresponsive strains identified novel molecular pathways conferring sensitivity or resilience to *DYRK1A* loss, and highlighted differential mRNA isoform usage as an important genetic determinant of response This cross-species strategy will be an powerful tool in the functional analysis of candidate disease variants identified through human genetic studies.

Teaser: Genetically diverse mouse embryonic stem cells provide a rapid approach to precision modeling of human disease.

Introduction

There is an increasing awareness of the importance of genetic diversity in cellular disease modeling, both for scientific reasons, and in relation to the issue of equitable access to biomedical innovations arising from *in vitro* discovery platforms[1]. The scientific benefits of genetic diversity in disease modeling extend to studies *in vivo*. Most mouse models for heritable human disorders have been created in a few commonly used inbred strains. However, genetic background can have profound effects on the phenotype of a particular mouse model. Thus, creating a gene knockout or mutation model on a single genetic background may or may not yield a phenotype relevant to human disease. This impediment to disease modeling has long been apparent from studies of mouse knockouts on different genetic backgrounds[2,3], and can generally be related to the effects of modifier genes[4].

To a considerable degree, incorporating greater genetic diversity into disease modeling in the mouse can provide a more reliable reflection of human disease pathogenesis than studies with a few inbred strains. A number of recent reports have shown clearly how the use of genetically diverse strain backgrounds can enhance our ability to model human sensitivity and resilience to disease, as exemplified in studies of Alzheimer's Disease, Type 2 diabetes, autism and gastric cancer[5-12]. However, the establishment, maintenance and use of mouse diversity panels requires significant infrastructure, animal husbandry, and genetics resources, limiting their implementation for many investigators.

In recent years, mouse embryonic stem cell (mESC) lines from genetically diverse mouse strains have become available, and they have been used *in vitro* to study the genetic basis of the permissiveness of strains for mESC establishment, the regulation of the pluripotent state and early lineage specification, and the stability of genomic imprinting *in vitro*[10-17]. To apply these approaches in disease modeling, it is important that differentiation protocols provide for similar high yields of relatively pure cell populations across genetically diverse cell lines. Here we report a novel paradigm for the application of genetically diverse mESC lines to *in vitro* disease modeling in the central nervous system (CNS), a precision neurogenetics approach that has the potential to make mouse genetic diversity more accessible to the research community, and to provide for facile selection of appropriate mouse genetic backgrounds for human disease modeling.

Experimental platforms based on human pluripotent stem cells (hPSC), including two-dimensional cultures and three-dimensional organoid models of specific brain regions, are playing an increasing role in the study of the development of the central nervous system, and in unraveling the genetics of brain disorders[18]. However, most neurologic or psychiatric disorders are highly complex, involving the interaction of multiple systems inside and outside of the CNS and behavioral phenotypes that cannot be observed *in vitro*. We aimed to provide a facile link between human disease models and mouse diversity genetics, to enable precision disease modeling. We first established a set of robust universal neural differentiation protocols that enable production of key CNS cells of interest from genetically diverse mouse inbred strains and hPSC. These protocols are applicable across mESC and hPSC representative of wide genetic diversity, encompass

multiple stages of neural development, and provide for functional readouts. Using high content screening, RNA-seq, electrophysiology, axonal regeneration paradigms, and knockout models, we provide a proof-of-concept study in the form of a chemogenomic and genetic analysis of the effects of loss of the neurodevelopmental gene, dual-specificity tyrosine phosphorylation-regulated kinase 1A (*Dyrk1a),* at multiple stages of neurogenesis and axonal repair. *Dyrk1a* was first discovered in Drosophila and the gene named "minibrain" because mutations in the gene causes size reduction of the optic lobes and central brain hemispheres[19]. *Dyrk1a* gene dosage affects many stages of neural development. In human, *DYRK1A* is located on Chromosome 21 and it has been associated with a range of conditions including Alzheimer's Disease, Down syndrome, microcephaly, autism, and intellectual disability[20-25]. Patients harboring the same point mutation in the *DYRK1A* gene display different phenotypes ranging from severe autism to relatively minor neurological impairment[24], strongly suggesting that the genetic background modifies the penetrance of the mutation.

Using genetically diverse mESC, we demonstrate the impact of genetic background on the outcome of DYRK1A inhibition or loss across multiple stages of neural development. With this approach, matching *in vitro* phenotypes in hPSC-based disease models with mESC models exhibiting similar sensitivity to pathogenic mutations enables rapid selection of mouse genetic backgrounds for *in vivo* modeling studies, and will provide a platform for prospective analysis of the power of *in vitro* mutant phenotyping to predict disease phenotype *in vivo,* a critical component of functional genomics analysis going forward.

Results

To achieve our objectives in precision disease modeling, we had to develop and validate *in vitro* methodology for the assessment of the effects of genetic variants on neural development and disease across eight highly genetically diverse mESC representing the founders of the Collaborative Cross (CC founders, A/J (AJ), C57BL/6J (B6), 129S1/SvlmJ (129), NOD/LtJ (NOD), NZOHiLtJ (NZO), CAST/EiJ (CAST), PWD/PhJ (PWD, in place of the closely related PWK/PhJ), WSB/EiJ (WSB)), and to carry out cross-species comparisons with hPSC. First, we developed universal differentiation protocols that functioned efficiently, then we tested the validity of our in vitro platform for its ability to predict how individual genotypes would respond to disease mutations.

Initially we trialed widely-cited differentiation protocols used to generate neurons from mESC[26-31] across a genetically diverse stem cell panel. These protocols failed when applied to strains other than 129. Therefore we developed the protocol shown in Fig S1a. With mESC from the B6 strain, by day 8 abundant neurites and neural rosettes are visible (Fig. S1b), and cells were passaged for expansion using EGF and FGF2 for three days. Decay in pluripotency markers and increase in neural markers were revealed by qPCR (Supplementary Figure 1c). At the end of this period, cells could be frozen, or passaged for further maturation by the withdrawal of mitogens and the addition of growth factors.

After the withdrawal of mitogens, NPCs exited the cell cycle and started to generate more elongated processes (Figure 1a). The timing of differentiation was similar across all strains (Fig. S2). After 7 days of differentiation, neurons represented around 90% of the overall cell population among all strains studied (Figure 1b,c). Among these neurons, glutamatergic cells represented around 75% of the neuronal population (Figure 1,d,e). Practically all neurons expressed the forebrain marker FoxG1 and cells expressing all individual six cortical layer markers were observed, across all strains analyzed strains at similar frequencies (Figure1b,e). We also analyzed the electrophysiological activity using whole cell patch clamp. Evoked action potentials were elicited as well as spontaneous activity, both appearing in cultures of all strains after 2 weeks of differentiation (Figure 1f) and coinciding with the presence of pre and post synaptic proteins (Figure 1d). Using multielectrode arrays (MEA) we found spontaneous field potentials (Figure 1g, upper panel) and network activity in all strains (Figure 1g, lower panel). We could also produce cortical organoids that displayed spontaneous calcium signaling (Figure 1h, i).

Modifications to the protocol, using morphogens to achieve patterning, enabled us to generate motor neurons, GABAergic neurons, and dopaminergic neurons from all strains tested at similar efficiencies (Figure 2). We reasoned that by adjusting the developmental timing between mouse and human cultures (Figure 3a), our protocol could be adapted to differentiate neurons from hPSC of diverse genetic backgrounds. We tested 10 genetically diverse hPSC from the iPSC Consortium for Omics Research (iPSCORE) representing equally both sexes and diverse ancestries. Once again, we were able to obtain neural progenitors and cortical neurons, and we found that all cell lines differentiated with similar efficiencies regardless of their genetic background (Figure 3b,c); we observed spontaneous synchronous electrical activity in these cultures (Figure

3d). With appropriate patterning (Figure 3e) we obtained motor neurons that also showed network activity (Figure 3f,g), as well as cortical and midbrain dopaminergic organoids that displayed spontaneous calcium signaling (Fig. S3,4 and Movie S1).

Having developed this differentiation platform, we proceeded to conduct a proof-of-concept study to examining how genetic background impacts on the effect of DYRK1A inhibition during neuronal development at different stages. *Dyrk1a* also regulates axonal growth and guidance, so we decided to assess an experimental model of axon regrowth as well. In most studies, we used the well-characterized DYRK1A inhibitor ID-8; this inhibitor is highly selective against DYRK1A compared to other kinases. ID-8 IC_{50} values for DYRK1A, GSK3b, and CLK1 are 78, 450, and 4200 nM respectively, and DYRK2, DYRK3, and DYRK4 are not affected at all[32-35].

To ascertain that differences in phenotypes observed in response to DYRK1a inhibition or haploinsufficiency were not merely a consequence of differences in gene coding sequences (and by extension protein structure) or expression levels across the strains, we examined both (Fig. S5). Despite some divergence in the gene sequences, notably for CAST and PWD (Fig. S5a), the SNV do not affect the protein sequence and all variants are synonymous (Supplementary Table 1). Examination of expression quantitative trait loci (eQTL), in mESC[14,36] revealed a local eQTL in CAST and PWD/K (Fig. S5b). Nevertheless, we could not find any protein QTL among all the strains in mESC, and direct measurement of protein levels in mESC revealed that although there is a slight decrease of DYRK1A protein in CAST, NOD, and PWD, these differences were not statistically significant (Fig. S5c,d,e and for neural progenitors, Figure 6 below).

Effects of DYRK1A inhibition on mESC maintenance and lineage specification vary across genetically diverse mouse strains.

It was previously shown that DYRK1A inhibition by ID-8 in mESC and hPSC helps to maintain the pluripotent state, and that either chemical inhibition or knockdown hampers specification from the pluripotent state to the neural lineage in hPSC[32,35]. In order to study pluripotency maintenance and lineage biases across mESC from different strains to compare with previous work on 129 mESC and hPSC, we cultured the eight mESC lines in media supplemented with four combinations of factors: LIF+2i (LIF plus PD0325901 and CHIR99021,optimal maintenance of naïve state mESC,[37]), LIF+ID-8, LIF, and ID-8. These cell lines were previously shown to vary in their response to LIF and in the stability of the undifferentiated state[14,38]; some lines remain in the undifferentiated state and others switch on lineage markers as soon as LIF+2i optimal conditions are abandoned, especially those mESC lines from strains regarded to be recalcitrant to stem cell derivation[13].

Using high content screening (HCS), we analyzed the expression of ten different pluripotency and lineage specific markers during four days of culture in the above conditions (Figure 4a,b). Only LIF+2i was able to maintain the expression of the pluripotency associated factors POU5F1, NANOG, and SOX2 in all cell lines; nonetheless, PWD and NZO expressed these markers at low levels under all conditions.

ID-8 was originally found to substitute for LIF in mESC maintenance on the 129 background [32]. Comparing cultures grown in LIF+2i with ID-8, we note that 129, AJ, and B6 show the best maintenance of NANOG expression in ID8 alone (Figure 4b, bottom panel). We also examined the proportion of cells expressing markers of the three embryonic germ layers (Figure 4b, top two panels). Those cell lines that showed consistent expression of pluripotency markers in ID-8 also showed low expression of most germ layer lineage markers. Colony morphometry using HCS provides another indicator of cellular response to the culture environment. Loss of stem cell marker expression generally correlated with changes in colony morphology, as morphometry showed that cell colonies became less compact and circular in ID-8 alone, and LIF+ID-8 enhanced roundness in 129 only (Figure 4c). Comparing LIF vs. ID-8 alone, the two conditions maintain pluripotency associated markers to a similar degree, but in 129, B6 and CAST, mesodermal markers are expressed at higher levels (Figure 4b,d). In summary these results confirm previous studies in 129 mESC and hPSC indicating that DYRK1A inhibition can help maintain the undifferentiated state. AJ and B6 derived mESC respond to ID-8 similarly to 129, but strains that are poorly maintained in LIF+2i are not rescued by DYRK1A inhibition.

DYRK1A inhibition differentially blocks neural progenitor proliferation in a strain-dependent fashion

Next, we used our differentiation system to study multiple stages in neural development, from neural lineage specification through to neurogenesis, neuronal differentiation, and maturation. For this, we differentiated the eight mESC lines into NPCs using our newly developed protocol in the absence or presence of ID-8, and analyzed the cultures at the beginning and on days two, five, and eight via immunostaining and HCS (Figure 5a,b). Following induction of neural specification in the presence of ID-8, B6 cultures contained lower percentages of OTX2 and TUBB3 positive cells, and displayed a marked reduction in the proportion of KI67 positive cells compared to control. Inhibition of the proliferation of neural progenitor cells during development is a hallmark of *Dyrk1a* haploinsufficiency. Further examination of the proliferation of neural progenitors from additional mESC clones of B6, AJ, 129 and WSB using KI67 and MCM2 immunostaining confirmed that the proliferation of B6 cells was strongly inhibited by ID8, whereas the latter three strains were unaffected (Figure 5c,d).

We previously observed an inhibition of neural specification in hPSC similar to that noted here[35]. We therefore examined the effect of heterozygous loss of *DYRK1A* on neural progenitor proliferation in the human induced pluripotent stem cell (hiPSC) line KOLF2.1J [39]. The susceptibility of B6 neural progenitor cells to inhibition of proliferation by ID-8 was mirrored in the reduced growth of *DYRK1A*+/- human iPSC neural progenitors relative to controls (Figure 5e). Thus, in terms of effects of DYRK1A inhibition on the maintenance of the undifferentiated state, interference with neural specification, and reduction of neural progenitor proliferation, the B6 mESC display the best face validity for modeling the response of human pluripotent stem cells to DYRK1A inhibition or haploinsufficiency.

To corroborate that the observed neural differentiation impairment is caused by ID-8-induced DYRK1A inhibition; we generated *Dyrk1a* knock-out mESC lines, specifically on B6, 129 and WSB backgrounds. We conducted NPC differentiation on these cell lines and analyzed the phenotype. Similar to results with chemical knockdown of DYRK1A, we observed that the only strain severely affected by *Dyrk1a* deletion was B6, whilst neural progenitor specification, proliferation and differentiation in WSB and 129 cell lines were indistinguishable from parental controls (Figure 6a,b). During B6 knockout cell line differentiation, we observed a decreased expression of proliferation and neural markers, and a decreased number of cells (Figure 6a,b). The proportion of cells expressing DYRK1A, and the intensity of staining, was similar in wild-type cells of all three strains (Figure 6b).

Although all strains had different degrees of response to ID-8 during neural progenitor specification and expansion, WSB was the most unresponsive while B6 was the most affected. Bulk RNA-seq was performed on these two cell lines at day eight of differentiation to identify the differences in gene expression associated with the extreme phenotypic differences found between WSB and B6. This difference in response to the inhibitor is evident from the numbers of differentially expressed genes (DEG); there were more than 700 DEG between B6 control and ID-8 treated cultures, but only 13 for control versus treated WSB (Figure 7a).

Regulatory transcriptional network analysis (RTNA) revealed *Foxb1*, *Hoxa4*, and *Hoxd3* as the top regulons associated with the differences found between WSB and B6 in response to ID-8 treatment (Figure 7b). *Foxb1* is a regulator of neural progenitor differentiation [40], and is rapidly and transiently induced during cortical specification of hPSC [41]. The two Hox genes are associated with hindbrain patterning in the CNS [42]. These pathways, not previously associated with *Dyrk1a* loss, are consistent with interference in neurogenesis and specific perturbations in hindbrain development (reported below) associated with *Dyrk1a* haploinsufficiency.

Gene ontology (GO) analysis indicated that either under control conditions or in the presence of ID-8, DEG associated with the response to LIF were highly overrepresented in B6 vs. WSB (Figure 7c, left panel). The LIF signaling pathway is responsible not only for maintenance of mESC but also for maintenance of mouse neural stem cells *in vitro* and i*n vivo* [43]. In the presence of ID-8, DEG associated with the GO term synaptic membrane were overrepresented in WSB relative to B6 (Figure 7c, right panel), consistent with progression of neural differentiation in the former but not the latter.

Using the RNA-seq data, we also analyzed gene isoform changes due to treatment and between B6 and WSB strains. Isoform usage can change considerably even when there is no overall change in gene expression, with functional consequences[44], and *Dyrk1a* is known to regulate the activity of a number of RNA splicing proteins[45-48]. Global analysis showed that adding ID-8 induced a loss of exons in B6 strain but not in WSB (Figure 7d). We found 200 unique genes with alternative isoform usage when control B6 cells were compared to WSB cells; an increase of variant isoforms between the two strains was observed in the presence of ID-8. (Figure 7e). Of particular interest was the finding that

Ntrk2 underwent a change in isoform expression in B6 NPC when treated with ID-8, whereas in WSB these isoforms remained unchanged (Figure 7f). *Ntrk2* codes for a neurotrophic receptor that binds BDNF. We found that ID-8 treatment induces a switch from the canonical isoform to an isoform lacking the kinase domain. This isoform is unable to transduce signaling via tyrosine phosphorylation, and it is notable that BDNF signaling was implicated in the response to *Dyrk1a* haploinsufficiency in a recent proteomics study in B6 mice[49]. That study did not investigate alternative splicing but the results are compatible with our findings.

These results suggest that, in the B6 strain in which neurogenesis is affected, DYRK1A inhibition interferes with multiple pathways involved in neural specification, patterning, and differentiation. RNA-seq confirmed the resilience of WSB against, and susceptibility of B6 to, DYRK1A inhibition at the neural induction stage. Subsequent analysis highlighted key pathways in neurogenesis downstream of DYRK1A inhibition, and identified a profound effect of DYRK1A inhibition on mRNA isoform usage. In the case of BDNF signaling, our results implicated alteration of isoform usage as an important genetic determinant of the response of neural progenitors to chemical knockdown.

DYRK1A inhibition delays functional maturation of neurons and modulates gene expression of maturation-related genes in a strain-dependent fashion

To understand how DYRK1A inhibition modulates physiological maturation of neurons, we used MEA plates capable of recording 16 field potentials per well on a 48-well plate to assess electrophysiological activity. We seeded young neurons and let them mature for six weeks while analyzing electrical activity at different time points (Figure 8a,b). Addition of ID-8 began two days after the NPCs were seeded and continued throughout. All cell lines were capable of generating action potentials and bursts of spikes, and creating networks, but not all cell lines matured at the same rate. CAST, B6, and 129 were the cell lines that matured the fastest, measured by Hz, bursting activity, and synchrony, while PWD took the longest (Figure 8a,b). We found that in most of the strains, addition of ID-8 inhibited the development of electrical activity; neurons fired less and bursts of activity were less frequent. Complementarily, interburst intervals, the relative silent time between two trains of activity, were longer for most cell lines when ID-8 was added. Quantitative analysis of a range of parameters at the peak point of control electrical activity (Figure 8b) confirmed inhibition of maturation across most strains by measurement of mean firing rate, number of bursts, prolongation of interburst intervals, and a reduction in spikes per burst. Two overall patterns were observed. In B6, CAST, A/J, and NOD, maturation was delayed and suppressed throughout the time course, whilst in PWD, 129, NZO, and WSB, maturation was delayed but activity recovered at the later time point (Figure 8b,c). Taken together, once again the functional maturation of neurons from B6 mESC was sensitive to ID-8, that of WSB mESC-derived cells were partially resistant to ID-8, and NZO derived neurons were the most resilient among all the strains. A decreased rate of functional network maturation is consistent with known effects of ID-8 on axonal growth and dendrite arborization.

We next performed RNA-seq on WSB and B6 neurons. Analysis at this stage showed a similar pattern to the NPC stage on the MDS plot which separates the neurons by strain and treatment; it also showed more distance between B6 subgroups than the WSB counterpart indicating B6 was more affected by DYRK1A inhibition (Fig. S6a). After ID-8 treatment, there were 220 DEG between WSB and B6 (Fig. S6b). GO analysis of DEG differentially affected by ID-8 in the two strains identified biological adhesion and transmembrane receptor signaling, with WSB showing a greater enrichment following ID-8 treatment (Fig. S6c). Cellular adhesion molecules are important for neural development and axonal growth [50]. *Rxrg*, *Dmrtb1*, and *Irf7* were the top regulons associated with the differences in response to DYRK1A inhibition between WSB and B6 neurons (Fig. S6d). *Rxrg* has been associated with neurodegeneration [51] and *Irf7* is a key mediator of the innate and adaptive immune responses [52] and positively regulates microglia polarization to the M2 state.

As we observed during neurogenesis, we also found more alternative splicing events in B6 compared to WSB neurons when treated with ID-8 (Fig. S6e). An example of this is *Slit2*, which exhibited isoform switches in B6 neurons when treated with ID-8 (Fig. S6f). *Slit2* is associated with axonal guidance and cell migration, and arborization[53]. All these developmental processes are affected by Dyrk1a mutations[54,55].

mESC strain differences in recovery from axonal injury in vitro reflect genetics of recovery from brain injury in vivo

There are marked strain differences in the ability of different mouse strains to respond to injury to the CNS [56]. Abundant evidence confirms that *Dyrk1a* plays a role during neurite sprouting in normal development, and that gene dosage alteration affects axonal growth and dendrite arborization[23], but it is not known whether these developmental roles of *Dyrk1a* might be recapitulated during axonal regeneration. As a further test of the predictive power of our *in vitro* system, we performed axotomy to analyze differences in axonal regrowth in neurons derived from mESC from CC founder strains.

We differentiated the mESC into neurons and cultured them into microfluidic chambers. (Figure 9a). On these devices, neurons were seeded on one chamber; axons could traverse microgrooves reaching into a second chamber whereas somas could not. After four days, axons grew through to the second chamber (Figure 9b). However, the number of axons growing through to the second chamber, and their length and density, indicated by the total area occupied by axons, varied amongst mESC strains (Figure 9c). At this point, axons were cut off and left to recover for four more days while treated or untreated with ID-8. In all cases, under control conditions, more axons grew across the device and had longer processes than before injury, except for B6 neurons (Figure 9b-d). CAST, NOD, and NZO grew significantly more following injury compared to all other strains. When ID-8 was added, most of the lines showed less growth than controls. WSB, AJ, and PWD axons occupied the same area after regrowth in the presence of ID8 as the control did (Figure 9d). WSB axons experienced the longest growth pre- and post-injury (both control and ID-8 treated). Notably, the extent of axon growth prior to injury was not

predictive of the extent of regrowth post injury (e.g. 129 versus NZO versus B6, Figure 9c).

Because of this divergent response to injury between B6 and WSB, we again undertook bulk RNA-seq analysis on these two cell lines to identify the underlying transcriptional differences. Interestingly, MDS analysis demonstrated vastly different responses between the two strains in the response to axotomy in the presence or absence of ID-8. As we saw from experiments in the maturation stage, ID-8 affected the transcriptome in both strains in control or axotomized cultures. However, when axons are severed, the B6 transcriptome showed limited change, irrespective of ID-8 treatment, whereas WSB transcriptome shifts markedly in response to axotomy in control and ID-8 treated cultures. The combination of ID-8 and axotomy displays an additive effect on the transcriptome in WSB, whereas in B6 this response is not observed, as axonal cut with or without ID-8 ("no drug") elicits the same effect (Figure 9e).

When axons were cut, the two cell lines (B6 and WSB) expressed a core set of genes. These genes were *Map11*, *Ntsr1*, *Ccn5*, *Slc16a3* and, *Smtnl2* reflecting GO associated with GO terms cellular response to hypoxia and neuron projection, both being part of a successful neuronal reaction to injury (Figure 9f). Top regulons for the differences found between the cell lines when injured were *Ascl1*, Creb5, and *Olig2* (Figure 9g). These transcription factors are important for neuronal differentiation and myelination. *Ascl1* has been associated with a superior regenerative capacity in dorsal root ganglion neurons in CAST versus B6 *in vivo* [57]. This differential expression pattern only emerged between the two strains after axonal injury.

After axons were cut and treated with ID-8, more genes were differentially expressed in WSB than in B6 (two-fold). Top common DEG genes in both cell lines were *Padi2*, *Calcr*, *Itgb4*, *Ifitm1*, *Npy*, *Tnfrsf11b*, *C1ra* and *Pcolce*; all of them are associated with axonal growth and guidance. In WSB-derived ID-8 treated neurons, gene sets associated with cell adhesion and central nervous system myelination were upregulated compared to the B6 counterpart (Figure 9h) and were confirmed by the number of hits per GO. This profile can explain a more robust axonal growth after axonal damage in WSB neurons. Finally, RTNA showed that two of the top three regulons associated with the differences in recovery after axonal growth, *Olig2* and *Ascl1,* were similar to those identified in the axonal damage response in the absence of ID-8. These results suggest that *Olig2*, *Creb5*, and *Ascl1* are part of the core regulatory network for a fast axonal growth after axonal damage when B6 and WSB are compared. Isoform switched analysis unveiled that *Ncoa4* was not only downregulated but also switched in isoforms was found after axotomy (Figure 9i). *Ncoa4* was recently associated with ferritinophagy and neurodegeneration [58].

A comparison of axonal regrowth of primary cortical neurons from P5 newborn B6 or WSB mice confirmed that the differences in growth post-injury seen in mESC derived neurons reflected the regrowth capacity of neurons isolated directly from the postnatal brain (Figure 9j).

427 Using all of the RNA-seq data, we analyzed the effect of ID-8 treatment independently of
428 the cell strain, and also compared across the two strains independently of the treatment,
429 throughout all stages analyzed. Analyzing effects of ID-8 in a strain independent fashion,
430 we found only 15 DEG genes, but the cross-strain comparison independent of treatment
431 found 261 DEG (Fig. S7a). Similar to the gene expression differences, differential use of
432 transcript variants were found between strains, and our data indicated that in general, the
433 consequences of isoform switches in B6 resulted in shorter transcripts (Fig. S7b). It is
434 worth pointing out that *Gapdh,* a housekeeping gene commonly used to normalize
435 expression data, was differentially expressed between WSB and B6 regardless of
436 treatment (Fig. S7c). This disparity could be associated with differences in metabolic
437 demands and energetic substrates. The latter correlates with differences we observed in
438 other ontologies like mitochondrial respiratory chain complex II assembly and
439 monocarboxylic acid metabolic process (data not shown). A gene set more enriched in
440 B6 independently of treatment was the regulation of apoptotic process involved in
441 development, whereas that a cerebral cortex development gene set was differentially
442 affected by ID-8, B6 being more severely affected (Fig. S7d). Gene sets enriched in WSB
443 relative to B6 in the presence of ID-8 included genes involved in cortex development,
444 forebrain development, and cell proliferation in forebrain, all in accordance with differential
445 effects on NPC proliferation in the two strains.
446
447 *Heterozygous loss of Dyrk1a is lethal on the B6 background but not on 129 or A/J*
448
449 Finally, we sought to establish the relationship between the *in vitro* susceptibility of B6 to
450 DYRK1A inhibition and the *in vivo* effects of *Dyrk1a* heterozygosity. We generated a null
451 allele of *Dyrk1a* by crossing female mice carrying the germline CMV-Cre to male *Dyrk1a*
452 mice carrying the conditional allele of *Dyrk1a* (floxed *Dyrk1a*) (Figure 10). When both
453 strains were on the B6 background, we did not recover any live pups heterozygous for
454 *Dyrk1a* deletion (*Dyrk1*a+/-) from this cross (0/93). We were able to obtain several mosaic
455 offspring for the floxed and deleted alleles, but crossing male mosaic mice to wild-type
456 B6 mice did not produce any live *Dyrk1a*+/- pups (0/46). Given that the prototype mouse
457 model of *Dyrk1a* haploinsufficiency was maintained on a mixed B6/129 background [59],
458 and our finding that B6 neural progenitors were uniquely sensitive to DYRK1A inhibition,
459 we reasoned that mice carrying the deleted allele may survive on a different background.
460 To test this idea, we crossed male mosaic mice to 129S1 female mice and obtained live
461 *Dyrk1a*+/- mice on a mixed 129/B6 background. We then backcrossed *Dyrk1a*+/- mice to
462 129S1 for six generations and found that heterozygote animals were born at Mendelian
463 ratios. We also mated B6 *Dyrk1* mosaic to AJ females, and live *Dyrk1a* heterozygous
464 pups were born. These results indicate that heterozygous deletion of *Dyrk1a* causes early
465 lethality on the B6 background but does not affect survival on the 129S1 or AJ
466 background.
467
468 We further examined the phenotype of *Dyrk1a*$^{+/-}$ mice on the 129B6F1 background.
469 Western blot analyses showed that the level of DYRK1A protein was reduced by half in
470 *Dyrk1a*$^{+/-}$ mice (Figure 10b). Mutant mice appeared smaller and weighed 25% less than
471 WT littermates during postnatal development and as young adults (Figure 10c,d).
472 Likewise, the brains of *Dyrk1a*$^{+/-}$ mice appeared smaller and weighed 30% less than those

473 of control littermates (Figure 10e,f), although the brain to body ratio was not significantly
474 changed. Brain histology indicated that the reduction in brain size was not uniform across
475 the brain, with the mid and hindbrain regions showing larger reductions than the cerebral
476 cortex (Figure 10g). These results corroborate previous findings that heterozygous
477 deletion of *Dyrk1a* in the mouse causes growth retardation and microcephaly, two key
478 clinical features associated with *DYRK1A* mutations in humans. *Dyrk1a*$^{+/-}$ mice on the
479 129B6F1 background also showed abnormal behaviors. In the open field apparatus,
480 *Dyrk1a*$^{+/-}$ mice were hypoactive compared with WT littermates (Figure 10h); they also
481 spent less time in the center of the arena than WT littermates (Figure 10i), suggesting
482 higher levels of anxiety in the mutant mice. Together, these findings confirm that
483 heterozygous deletion of *Dyrk1a* on an appropriate genetic background recapitulates key
484 features of human disease phenotypes, and that the B6 genetic background confers
485 extreme sensitivity to the haploinsufficiency syndrome in the mouse.

Discussion

To facilitate genetic analysis *in vitro* of neural development across a diverse range of mouse genetic backgrounds, we developed a new protocol to differentiate pluripotent stem cells into neurons from genetically diverse mESC and hPSC. We demonstrated the applicability of this model in analyzing the effects of chemical knockdown or genetic ablation of the activity of a key neurodevelopmental gene throughout neurogenesis and neural maturation and repair, and we were able to demonstrate how the knockdown phenotype varies dramatically depending on the genetic background.

The studies described here address three key questions in precision disease modeling. The first has to do with bridging the gap between *in vitro* studies and disease models in whole organisms, and asks, can disease modeling in genetically diverse mouse embryonic stem cells tell us what mouse strains are most representative of human phenotypes, and thus guide the choice of strain for whole organism studies? The second, a more general question of widespread significance, asks can any stem cell-based platform yield reliable information about the sensitivity or resilience of a particular individual genotype to pathogenic mutations? And the last question asks, does comparisons of *in vitro* phenotypes from stem cell models in sensitive and resilient strains yield reliable information about molecular pathways that might be critical to response to disease mutations in vivo?

Our studies have revealed that at most stages of this study, from embryonic stem cell renewal to neural specification, neurogenesis, and neural maturation and repair, B6-derived cultures were responsive to DYRK1A inhibition or loss while most other strains proved less sensitive. It is notable that C57BL/6J mice or hybrids thereof have been used successfully in a number of studies to model the effects of DYRK1A haploinsufficiency in human. Thus, on a C57BL/6J, 129S2/SvHsD mixed background, *Dyrk1a*$^{-/-}$ mice show developmental delay and reduced brain size with greatly reduced neuronal content and die at mid-gestation[59]. Heterozygotes on this background have fewer intermediate neural progenitors in the subventricular zone at E11.5-13.5 owing to proliferative defects[60]. In the adult animal, cortical pyramidal neurons are smaller, and show less branching and fewer spines[61], and neural progenitor maintenance in the subventricular zone is impaired[60]. These same animals show decreased cognitive abilities[62]. *Dyrk1a*$^{-/+}$ mice on a pure C57BL/6J background also show reduced brain size and cognitive defects[63]. Conditional knockout of *Dyrk1a* in the cortex of C57BL/6J mice was lethal in homozygotes; homozygotes and heterozygotes showed microcephaly related to reduced proliferation of neural progenitors in the immediate postnatal period, and a decreased complexity and reduced branching of cortical neurons[49]. We could not generate any heterozygous mouse on a pure C57BL/6J background, and only when it was crossed with less susceptible strains could we obtain heterozygous mice that showed similar effects to those described by other authors. Levy et al.[49] used a cortex-specific KO approach which spared the remaining brain and body of the deleterious effects of the KO, making this intervention potentially less lethal. Raveau et al.[63] used a strategy that was not tissue-specific, but the target region for the frameshift was upstream of the NLS and in exon 3, whereas in our case it was downstream of the NLS and the kinase domain was targeted.

532 It is possible that in our model, the remnant N-terminal peptide can cause a dominant-
533 negative effect generating a more severe phenotype, or that, in the study of Raveau et
534 al., exon skipping resulted in a protein with partial activity[63]. Interestingly, the observation
535 that *Dyrk1a*$^{-/+}$ had smaller midbrain and hindbrain in our *in vivo* study correlates with
536 aspects of our findings *in vitro*. We found that B6-derived NPCs treated with ID-8 had a
537 decreased expression of *Hoxa4* and *Hoxd3*, homeotic genes associated with hindbrain
538 development. Altogether, our results indicate an impaired development of the hindbrain
539 at an early stage of neural differentiation unveiled by our *in vitro* analysis that otherwise
540 would have been difficult to pinpoint.
541
542 Our previous work showed that neural specification of human pluripotent stem cells was
543 blocked in *DYRK1A* knockdown or in ID-8 treated cells[35]. Here, we showed that the
544 proliferative capacity of neural progenitors derived from *DYRK1A* +/- hPSC was reduced
545 relative to controls. We observed both phenotypes in mESC or mESC-derived neural
546 progenitors from B6 mice. These findings as well as the data discussed above show that
547 our *in vitro* results correctly identify the B6 mouse as a sensitive model for the effects of
548 *DYRK1A* haploinsufficiency in the human. By contrast, other strains were unresponsive
549 to the developmental effects of DYRK1A inhibition. We also corroborated the effects of
550 chemical DYRK1A inhibition by conducting knockout experiments demonstrating that the
551 deleterious effect of DYRK1A inhibition is strain dependent. Although *DYRK1A* is subject
552 to strong constraint in the human, and most heterozygotes show impairment of neural
553 development, the severity of clinical phenotypes in individuals hemizygous for loss of the
554 gene varies quite considerably[24,64]. Further *in vitro* analysis of mESC derived from
555 recombinant inbred strains representing sensitive and resistant genetic backgrounds (B6
556 and 129 respectively) could identify key modifier genes, and potentially target pathways
557 for therapeutic intervention during the early life of affected individuals. One such target
558 is the BDNF signaling pathway, which we and others identify as a critical downstream
559 modulator of *Dyrk1a* haploinsufficiency.
560
561 We also examined the effects of DYRK1A inhibition on axonal regrowth across the eight
562 strains in our study. While repair and plasticity in the adult CNS often encompass some
563 features of neurodevelopmental pathways, development and repair in the CNS are not
564 driven by identical processes[65]. Our observations showed that the extent of axonal
565 regrowth after injury in neurons derived from mESC does not directly relate to the extent
566 of growth before injury across the mESC lines examined, suggesting that indeed axon
567 growth during development and repair are different even in relatively immature neurons.
568 There were large differences in the ability of axons derived from mESC of different strains
569 to regrow in this assay. Importantly, the robust regrowth of neurons derived from the
570 CAST strain contrasts strikingly with the poor regrowth of neurons derived from B6 mESC.
571 Our observation of poor axonal regrowth in primary cultures of cortical neurons from P5
572 B6 or WSB mice confirmed the results obtained on neurons derived from mESC. In a
573 number of studies *in vivo*, B6 mice have been shown to display deficient axonal
574 regeneration relative to 129 or CAST [66-71], deficiencies that have been attributed either to
575 variation in the inherent capacity for axonal repair or differences in the extent and nature
576 of inflammatory responses in the various strains.
577

578 Comparison of gene expression in B6 and WSB strains that were sensitive or relatively
579 resistant to effects of DYRK1A inhibition across different developmental stages revealed
580 the power of the mESC model to identify novel critical molecular pathways and networks
581 that are altered by genetic deletion of *Dyrk1A in vivo*. At the stage of neurogenesis,
582 analysis of DEG highlighted the LIF pathway, which is a major regulator of neural
583 progenitor proliferation *in vivo* not previously associated with Dyrk1a haploinsufficiency.
584 RTNA found that networks related to *Foxb1*, a gene critical in the regulation of neural
585 progenitor proliferation, were differentially active in the two strains. RTNA also identified
586 two HOX genes involved in hindbrain development as targets of DYRK1A loss of activity
587 in the B6 sensitive strain, consistent with phenotype data from B6/129 hybrid animals.
588 Analysis of the expression of splice isoforms showed global changes in the presence of
589 ID-8, in line with the known interactions of DYRK1A with splicing factors, and highlight
590 alterations in splicing as an important determinant of susceptibility to *Dyrk1a*
591 haploinsufficiency. The shift in isoform usage of the BDNF receptor *Ntrk2* to a form
592 encoding a protein lacking the kinase domain in the presence of ID-8 in B6 neural
593 progenitors could explain the downregulation of the BDNF pathway activity observed in a
594 proteomics and phosphoproteomics study of conditional knockout of *Dyrk1a* in the cortical
595 neurons of C57BL/6J mice[49]. Our studies of axonal repair identified the *Ascl1* regulon as
596 a major differential response to injury in both strains either with or without DYRK1A
597 inhibition. In a model of peripheral neuron (dorsal root ganglion) repair, Lisi et al. [57] noted
598 a differential upregulation of *Ascl1* in CAST (identified by these authors and by our study
599 as a good regenerator compared to B6) relative to B6. These authors also used
600 overexpression and knockdown studies to confirm a role for *Ascl1* in axon regrowth. In
601 summary, our *in vitro* studies comparing gene expression in strains sensitive and resistant
602 to DYRK1A inhibition corroborate *in vivo* data on key molecular pathways involved in
603 neuronal development and repair and their perturbations in *Dyrk1a*-deficient animals.
604
605 In our comparison of gene expression in both strains across all stages, the finding that
606 *Gapdh* was the highest DEG was surprising, because it has been widely used as a
607 reference housekeeping gene, with some studies supporting such use[72] and others
608 reaching the opposite conclusion[73]. GAPDH induces apoptosis when translocated into
609 the nuclei of both neural and non-neural cells, and it shows dynamic changes in
610 neurodegenerative diseases, cancer, and hypoxia[74,75]. GAPDH acts a sensor of NO
611 stress[76], and participates in dendrite development[74,75,77]. The strain differences we
612 observed in *Gapdh* expression could have broader implications for disease modeling in
613 B6 mice.
614
615
616 The approach we describe here could be generalized to address a range of issues in
617 modeling the genetics of disease. Screening approaches using shRNAi or sgRNA
618 CRISPR methodologies are also applicable in this system. We readily applied high
619 content screening and medium throughput microelectrode array methodologies in our
620 work. The small panel of mESC used in this study incorporates wide genetic diversity,
621 but we are also developing mESC or iPSC panels from Diversity Outbred mice and from
622 recombinant inbred strains. These mESC genetic diversity panels have been used for
623 quantitative trait loci analysis, and could be used for rapid mapping of modifiers that

influence phenotypes of genetic variants implicated in neurodevelopmental disorders. Identification of modifier genes could yield new leads for drug discovery and early intervention in patients. We focused here on neural development, but this same approach could be applied to any lineage or tissue that can be generated from pluripotent stem cells. Facile comparison between phenotypes of human and mouse pluripotent stem cell models *in vitro* will aid in the identification of those mouse genotypes that confer sensitivity or resilience to disease variants, providing for more precise disease modeling *in vivo* and reducing the experimental use of animals.

Finally, most disease modeling studies using hPSC have been retrospective, replicating the known effects of disease mutations to varying degrees in a culture dish. The use of hPSC and mESC in parallel followed by *in vivo* studies in the mouse provides a means for prospective testing of the ability of *in vitro* screens to predict the effects of genetic variants *in vivo*. This will be an important adjunct to hPSC studies aimed at validating novel candidate disease variants emerging from genetic studies in humans. Such a strategy will add considerable power to functional genomics analysis of variants of unknown significance, or variants for which the role in pathogenesis of disease is undefined. For such variants, establishing a link between observations in cell culture models and precision modeling *in vivo* will be essential.

Limitations and future directions: We acknowledge that we did not investigate the gender effect in our study and all stem cells are male-derived. Although ASD has a higher rate of affected males, and *DYRK1A*mutation is one of the causes of ASD[78] ; *DYRK1A* haploinsufficiency syndrome does not seem to have a gender bias[79]. Evaluations of sex-dependent effects can be performed using female-derived stem cells, which are availabel from our laboratory; nonetheless, this is out of the scope of this paper. Also, we found that although our protocol can efficiently differentiate genetically diverse stem cells ot mature neurons, electrical maturation is achieved at different time rates as proven by our MEA recordings. Recently Hergenreder et al. https://doi.org/10.1101/2022.06.02.494616 reported that a small molecule cocktail can accelerate neuronal maturation. Addition of these molecules might synchronize the maturation rate of NPCs from genetically diverse stem cells.

Materials and Methods

RESOURCE AVAILABILITY

LEAD CONTACT

Further information and requests for resources and reagents should be directed to and will be fulfilled by the lead contact, Martin Pera (martin.pera@jax.org).

MATERIALS AVAILABILITY

Dyrk1a$^{-/-}$ mESC strains are available from our laboratory.

DATA AND CODE AVAILABILITY

- Bulk RNA-seq data have been deposited at GEO and are publicly available as of the date of publication. Accession numbers are listed in the key resources table.
- This paper does not report original code.
- Any additional information required to reanalyze the data reported in this paper is available from the lead contact upon request

EXPERIMENTAL MODEL AND SUBJECT DETAILS

ANIMALS

Experiments were conducted in accordance with the guidelines of the Institutional Animal Care and Use Committee (IACUC) of the Jackson Laboratory. For axonal injury/recovery experiments in postnatal neurons, postnatal mice (p3-p5) from C57BL/6J and WSB/EiJ strains were sacrificed by decapitation and cells prepared according to the method below (Preparation of p5 NPC for axonal damage experiments).

CELL LINES

mESC from the CC founders[80] were used; however, PWD/PhJ was substituted for PWK/PhJ. All mESCs were kept and used under ten passages to avoid chromosomal rearrangements. All mESCs are male, germ competent, negative for mycoplasma, and retain a normal karyotype. mESC media comprised Knockout DMEM, 15% Fetal calf serum, 2 mM Glutamax, non-essential amino-acids, 50 units/ml Penicillin, 50 μg/ml Streptomycin, 55 μM beta-mercaptoethanol, and 1000 IU of Leukemia inhibitory factor. Cells were grown on gamma-irradiated mouse embryonic fibroblast feeder cells at 37°C and 5% CO2. mESCs were passed using Trypsin 0.25%

KOLF2.1J hiPSC was used for neural differentiation studies comparing WT and heterozygous knock-out cells. CRISPR-Cas9 was used to produce frameshift mutants in Exon 2 on one allele of the *DYRK1A* gene, generating Dyrk1a +/- mutants, as previously described[81]. Cells were maintained on vitronectin-coated dishes in Stemflex media (Stem Cell Technologies) and passed using ReLSR (Stem Cell Technologies). hPSCs were kept and used under ten passages to avoid chromosomal rearrangements. hPSCs used in this study were karyotyped for chromosomal abnormalities and mycoplasma tested.

METHOD DETAILS

Cortical neuron differentiation of mESC

mESC were cultured as described above. Upon reaching 80% confluency (day 0), cells were trypsinized and seeded on a culture dish for an hour to let feeders attach to the dish. Unattached

mESC were recovered and counted. EB were formed by seeding 3E5cells on a well of a 6-well plate (ultra-low attachment) in mESC media (described above in “CELL LINES”) plus 10 μM SB431542 and 1 μM Dorsomorphin. The next day (day 1), the EB-containing media was transferred to adherence; previously, a well of a 6-well plate was coated with 100 μg/mL Poly-Lysine (PLL) for 2 hours and then treated with, 1 μg/mL laminin (Lm), 5 μg/mL fibronectin (Fn) for at least two more hours. After 24h (day 2) of seeding the EB on adherance, media was removed and switched to NMM (Gaspard et al., 2009) (Neurobasal and DMEM/F12 1:1 vol/vol) plus SB431542, Dorsomorphin, 2 μM I-BET151, and 5 μM retinoic acid. 24h later (day 3), media was removed, and fresh NMM plus SB431542 and Dorsomorphin were added. The next day (day 4) SB431542 and Dorsomorphin were withdrawn for B6 and WSB, while the other strains were maintained on SB431542 and Dorsomorphin for two more days (until day 6) after which the inhibitors were withdrawn. Thereafter, all cells were kept on basal media (NMM) with daily media changes until day eight, when cells were passed to the NPC expansion stage (day 8 to 11). Dissociation of cells into small clumps was done using Tryple Express and expanded at a 1:2 split ratio on PLL/Fn/Lm-coated dishes in NMM plus 20 ng/mL FGF2, 20 ng/mL EGF, and RevitaCell (Gibco). After 24 hours (day 9), Revitacell is removed but mitogens are daily added for two more days. At day 11, cells were dissociated with Tryple Express to yield a pure population of NPC. NPCs were frozen using Knockout Serum Replacement and 10% DMSO, or passed onto a newly coated plate for neuronal maturation using adult NMM media (formulated with Neurobasal A in place of Neurobasal medium), plus Revitacell, 10 ng/mL GDNF, 10 ng/mL BDNF, and 10 μM Forskolin. Next day (day 12) Revitacell was removed. Three days later (day 15), Forskolin was removed and 5 μM 5-fluorodeoxyuridine was added for one week (until day 22). After that, adult-NMM + GDNF and BDNF was changed twice per week.

GABAergic differentiation of mESC

The first four days of differentiation were carried out as described in the cortical differentiation protocol above. On day five, SB431542 and Dorsomorphin were removed, and fresh media was added. On day six, a sonic hedgehog agonist (SAG, 10 μM) was added with every media change and withdrawn after three days of neuronal differentiation. The rest of the protocol was exactly the same as the cortical differentiation.

Dopaminergic differentiation of mESC

This procedure was the same as described for GABAergic neurons until day six. On this day, SAG and FGF8 (100 ng/ml) were added for two days, at which point conversion to NPC had occurred. Cells were passed as previously described, with the addition of Revitacell, FGF2, non-essential amino acids, FGF8, SAG1, IWP2 (1 μM) and LY364947 (3 μM) during the expansion stage. After plating cells for maturation, Revitacell, 10 μM Forskolin, BDNF, GDNF, 50 μg/ml ascorbic acid, CHIR99021 (3μM) and LY364947 were added. Media was changed on the third day with the continued addition of BDNF and GDNF. The cortical neural protocol was followed after day four of neuronal differentiation.

MN differentiation of mESC

Differentiation was as described for cortical neurons until day seven. On day four, SAG and retinoic acid were added with every change media. On day seven, neurons emerged and cells were ready to be seeded as young MN. When passing the cells, Revitacell, Forskolin, BDNF, GDNF, SAG1 and RA were added. After three days, all the small molecules were withdrawn and

BDNF and GDNF were retained. After this point, half of the media volume was changed two to three times per week

Cerebral organoid differentiation of mESC

The protocol for organoid formation was based on the cortical differentiation protocol above. Briefly, 2000 cells were seeded per well of a round bottom, ultra-low attachment, 96-well plate in mESC basal media with LIF, SB431542, and Dorsomorphin. Forty-eight hours later, the spent media was removed and replaced with NMM+ SB431542, Dorsomorphin, I-BET151 and retinoic acid. The next day, this medium was removed and NMM with SB431542 and Dorsomorphin was added. Forty-eight hours later, half the volume of the culture medium was replaced. At day six and eight, half of the media was replaced with basal media (NMM). On day ten, organoids were split evenly and 24 organoids were placed into 6 cm ultra-low attachment dishes. On day 16, organoids are embedded in undiluted Matrigel (Corning, 356234) in the same medium and kept on a shaker at 16 rpm for at least 21 days.

hPSC-derived NPC

The protocol was the same as the one used for mESC with a few modifications . IBet151 and RA were added at day one instead of day two (still 24h treatment). SB431542, and Dorsomorphin were added until day eight. From day eight to eleven, cells were kept in basal NMM media. At day 11, the differentiated NPCs were passed and expanded using bFGF and EGF for three days. Afterwards, cells were frozen or used for further experiments.

hPSC Neurosphere assay

Human NPC were seeded on a 96-well ultra-low attachment plate at various concentrations (2, 8, 16 and 32 thousand cells) for 15 passages in NMM + FGF2 and EGF. Media changes were performed every other day. Spheroids were imaged with a Leica Dmi1 microscope and their size calculated using ImageJ software. Spheroids were passed every 4 days using Accutase for 30min at 37°C.

EdU labelling of NPC

Cells were incubated for 2 hours with 5μM EdU. After 48 hours, cells were harvested and fixed with 4% paraformaldehyde at room temperature for 15 minutes. EdU incorporation was detected according to the Clik-iT EdU Alexa Fluor 594 flow cytometry assay kit protocol. Cells not labelled with EdU were used as negative control.

hiPSC-derived cortical neurons

The protocol was similar as the one used for mESC but with slight modifications. Cells were dissociated with Accutase. 5E5 cells were seeded on a well of a low-attachment 6-well plate in the presence of SB431542, Dorsomorphin, Ibet151, RA, and Y-27632. 24 hours later, EB were sedimented under unit gravity, the media was removed, and 4 ml mTeSR plus media supplemented with SD434512 and Dorsomorphin was added. EB were seeded in a PLL/Fn/Lm

801 coated well of the same size and incubated for 24 hours, after which the medium was replaced
802 with NMM + SB and Dorsomorphin. This medium was changed every day until day 11, at which
803 point small molecules were withdrawn incubation with basal media continued for 3 more days.
804 Cells were dissociated into clumps of cells and reseeded at a 1:2 split ratio on PLL/Fn/Lm coated
805 dishes in the presence of bFGF and EGF for two or three days for NPC expansion with the
806 addition of Rock inhibitor during the first day. NPC can be frozen as with the mESC, or cells plated
807 for neuronal differentiation, but 5FDU is added for seven days.
808
809
810 Differentiation of hPSC into motor neurons
811
812 Cell were differentiated according to the hPSC to cortical neuron protocol with minor
813 modifications. On day eight, retinoic acid and SAG were added, and cells were maintained in this
814 medium until day 23. Every time cells were passed, 5 μg/ml each of Fibronectin and Laminin were
815 supplemented in the media in addition to their usage in the plate coating; these were
816 supplemented again twice per week to avoid cell detachment and until 10 days after withdrawal
817 of mitogens.
818
819 Differentiation of hPSC into Cerebral organoids
820
821 Initial differentiation was similar to 2D cortical cultures, but adapted for organoids by culturing in
822 suspension, embedding in Matrigel and growth under agitation. Four thousand iPSCs were
823 seeded in 100 μl of media per well of a 96 well plate with all aforementioned molecules.The
824 following day, cultures were switched to mTeSR plus with SB and Dorsomorphin. Next day this
825 medium was replaced with IDM (DMEM-F12 glutamax and Neurobasal 1:1 vol/vol ratio, N2
826 supplement, 5μg/ml insulin, non-essential amino acids, Penicillin-streptomycin and B27
827 supplement without Vit A) with SB and Dorsomorphin. This medium was changed every other day
828 until day 11. At this point the organoids were embedded in Matrigel. The cultures were incubated
829 in 6 ml of media overnight, and on the following day, transferred to to an orbital shaker with an
830 orbit of 1.9 cm (0.75 inch) at 69 rpm. On day 18, half the media volume was replaced with fresh
831 media. On day 20, Matrigel was removed and the medium switched to NMM. From then on, the
832 media was changed two to three times a week. On day 30 cultures were switched to A-NMM adult
833 with media changes two to three times per week.
834
835
836 Differentiation of hPSC into Dopaminergic organoids
837
838 Adaptation of the cortical organoid differentiation protocol was done as follow. SAG was added
839 from day 4 until day 11 when it was withdrawn. FGF8 was added from day 6 until day 11 when it
840 was withdrawn. LY36947 and IWP2 were added at day eight until day 11 and 15
841 respectively.CHIR99021 and Ascorbic Acid were added on day 11 until day 15 and day 30
842 respectively.
843
844
845 Calcium spike assay
846
847 Organoids were assayed using the FLIPR Calcium 6 assay kit (Molecular Devices). Briefly,
848 organoids were incubated for two hours in half FLIPR Calcium 6 reconstituted reagent and half
849 NMM media. Afterwards, this medium was removed and fresh media was added. Organoids were
850 immediately transferred to Opera plus microscope (Perkin Elmer) under controlled environmental
851 conditions (37C and 5% CO_2 in a humidified chamber). Images were taken every 0.7 seconds up

852 to 400 frames. Calcium spikes were analyzed using the integrated Harmony software by
853 recognizing individual cells and tracking fluorophore intensity over time.
854
855
856 Electrophysiological Recordings
857
858 NPC were seeded on a previously coated MEA plate and left to mature as described above.
859 However, for the MEA plates, a 10 μl droplet containing 50,000 mouse NPC or 20,000 human
860 NPCs was seeded at the center of each well of a 48-well plate (CitoView MEA 48, Axion
861 biosystems). After cells have attached (≈7h), more media was added to properly cover the well.
862 Recordings were obtained on day 7, 14, 21, 28, 35, and 42. Spontaneous activity was recorded
863 on an Axion Maestro Pro at 37°C for 10 minutes using the AxiS navigator software. Recordings
864 were analyzed using the built-in spike detector at 6 x STD.
865
866 Axonal Damage using mESC-derived neurons
867
868 NPC of each cell line were seeded on one of the two chambers of a microfluidic device (ENUVIO).
869 Devices were pre-coated with PLL/Fn/Lm. Cells were left to mature for four days. Afterwards, in
870 the contralateral chamber, axons were cut off by scratching the chamber and pipetting the media
871 up and down several times. The axonal chamber was rinsed to removed debris and replenished
872 with fresh media and Fn/Lm to enhance axonal attachment. Four days later, the axonal side was
873 treated with Calcein AM, and images of the entire device were taken. The area covered by axons
874 was analyzed using ImageJ.
875
876 Preparation of p5 NPC for axonal damage experiments
877
878 C57BL/6J (B6) and WSB/EiJ (WSB) postnatal day five animals were euthanized as described
879 above. The hippocampus/dentate gyrus was dissected, mechanically dissociated, and seeded on
880 PLL/Fn/Lm-coated dishes in NMM media plus EGF and FGF (20 μg/ml each) and expanded
881 through one passage. At this point, expanded NPC were used for axonal damage experiments in
882 the same fashion as mESC-derived NPCs described above.
883
884 Immunostaining
885
886 Cultures were washed with PBS and fixed with 4% paraformaldehyde 4% for 15 min and finally
887 washed again with PBS three more times. Blocking and permeabilization were carried out using
888 5% BSA and 0.3% Triton-X for an hour at room temperature. Primary antibodies used were OTX2,
889 Millipore AB9566-1 (1:1000); TUBB3, Biolegend 801202 (1:1000); Ki67, Santa Cruz SC-23900
890 (1:50); PAX6, Biolegend 862001 (1:1000); Brachyury, R &D systems AF2085 (1:200); Vglut,
891 Abcam ab104898 (1:200); CHAT, Merck Millipore AB144P (1:200); Hb9, Thermo PA5-67195
892 (1:200); MCM2, Abcam ab95361 (1:500); DYRK1A, cell, signaling, (1:1000); ISL1, DSHB 40.3A4-
893 S and 40.2D6-S both undiluted 1:1; SOX2, Millipore AB5603 (1:500); Eomes, Abcam ab23345
894 (1:1000); POU5F1, BD 611202 (1:500); GATA4, Santa Cruz SC-25310 (1:2000); NANOG,
895 PeproTech 500-P236-50UG (1:500); SOX1, R & D AF3369-SP (1:500); AFP, Dako A0008
896 (1:500); GFAP, Dako Z0334 (1:1000); NeuroD1, Abcam ab60704 (1:2000); TH, Pel-Freez
897 P41301 (1:1000); GAD 65/67, Millipore ABN904 (1:250); vgat, Synaptic systems 131011 (1:200);
898 Reelin, Abcam ab78540 (1:200). Primary antibodies were incubated overnight, washed three
899 times with PBS and secondary ALEXA antibodies (1:1000) against primary antibodies were
900 incubated for two hours. DAPI was used for nuclear counterstaining. Cerebral organoids were

901 cleared and stained using fructose-glycerol clearing method (Dekkers et al., 2019) and antibodies
902 were used at twice the concentrations described above.
903
904 High content microscopy
905
906 Perkin Elmer cell carrier ultra 96-well plates were used for high content microscopy. Imaging was
907 carried out on the Operetta CSL (Perkin Elmer) microscope, and image analysis was done using
908 Harmony software.
909
910 RT-PCR
911
912 Samples were collected and RNA was prepared using Qiagen RNAeasy plus mini kit (Qiagen).
913 Reverse transcription was carried out using High-Capacity RNA-to-cDNA™ Kit (ThermoFisher).
914 Real-time PCR was conducted using Quantstudio 7 Flex on a 2-step cycle run using Taqman
915 Probes (Oct4, # 4331182; Nanog, #4331182; Otx2, #4331182; Pax6, #4331182; Tubb3,
916 #4351372; Scl17a7, # 4331182; Gapdh, # 4453320).
917
918
919 Bulk RNA-seq
920
921 Samples were collected and RNA was prepared using Qiagen RNA column system. mRNA
922 libraries were made at 150 x2 with at least 30 000 reads per sample.
923
924 Transcriptomic analysis
925
926 Low-quality bases (Q < 30) from the 3' end of reads were removed and reads with more than 30%
927 low-quality bases (Q < 30) overall were filtered out. Trimmed reads were aligned to the reference
928 genome using bowtie2 [82], generating a bam file which was used by rsem for quantification
929 providing expression counts for genes and isoforms separately. Quality metrics were obtained at
930 the fastq and bam level. This includes metrics such as total number of reads, total number of high-
931 quality reads and alignment rate. The RNA-seq data was filtered and normalized. MDS plots
932 were made using EdgeR [83]. Venn diagrams were made using systemPipeR [84] and the Limma [85]
933 package was used for barcode plots and testing for multiple gene sets. Gene ontology analysis
934 and plotting was completed using TopGO [86] and GO.db [87]. Transcriptional network analysis was
935 done using RTN [88]. Circos plots were made using circlize [89]. Isoform switching was analyzed
936 using IsoformSwitchAnalyzeR package [90] and other tools to import data, conduct normalization,
937 isoform switch testing, prediction of open reading frames, premature termination decay, coding,
938 domaings signal peptides, protein disorder and consequences [90-96]
939
940
941 Statistical analysis
942
943 Statistical details can be found within the figure legends. Computation and plots were done using
944 Rstudio and GraphPad Prism.
945
946

SNP and transcript variant analysis

Dyrk1a sequences were pulled from the mouse genome project (https://www.mousegenomes.org/) and compared for number of SNPs and transcript variants per strains. Sequence variants were aligned using Clustal O multiple sequence alignment. Sequences downloaded from https://www.informatics.jax.org/mgv/

QTL analysis

Diversity outbred (DO) mouse embryonic stem cell (mESC) expression quantitative trait loci (eQTL) and protein QTL analysis are previously published (Skelly et al,. 2020 and Aydin et al., 2023)andavailableat (https://churchilllab.jax.org/qtlviewer/DO_mESC and https://doi.org/10.6084/m9.figshare.22012850). Data for Dyrk1a was accessed through publicly available data sources. QTL mapping was performed using a linear-mixed model implemented in the 'scan1' function in R/qtl2 package with rank normal scores, sex of the cell lines as an additive covariate and the leave one chromosome out option for kinship correction (citations for R/qtl2 and DOQTL).

Western blot

Cells were lysed with NP40 cell lysis buffer supplemented with Protease Inhibitor Cocktail-P2714, Sigma. Cells were centrifuged for 15 min at 12,000g at 4°C. Supernatant was saved and kept frozen until further use. DC protein assay (Bio-Rad) was used to quantify protein. The cell lysate was placed in SDS sample buffer and run in a pre-casted gel at 100V. Proteins were transferred into nitrocellulose using the trans-Blot turbo (BIO-RAD). Primary antibodies are described above. Secondary antibodies were goat anti-Rb HRP (Abcam ab6721, 1:10,000) and horse anti-moouse (Vector Labs PI-2000-1). Detection was performed using SuperSignal Atto (Thermo) using a G box documentation system (Syngene).

Generation of *Dyrk1a* null allele

Mice carrying *Dyrk1a* null allele were generated by mating male mice homozygous of conditional *Dyrk1a* floxed allele (JAX Strain #027801) with female mice hemizygous of the germline CMV-Cre (JAX Strain #006054). Both strains were on a B6 background. Genotyping was performed by PCR on tail DNA. The PCR primers for Dyrk1a alleles are: forward 5'-CCT GGA GAA GAG GGC AAG-3' (common), reverse 5'-GGC ATA ACTTGC ATA CAG TGG-3' (wild type and floxed allele), and reverse 5'-ACT GTG TGA GGA GTC TTG ACA-3' (null allele), which give products of 132, 232 and 295 bp for wild type, floxed, and null allele, respectively. The PCR primers for CMV-Cre are: forward 5'-GCA TTA CCG GTC GAT GCA ACG AGT GAT GAG-3', reverse 5'-GAG TGA ACG AAC CTG GTC GAA ATC AGT GCG-3', which gives a product of 410 bp for the transgene.

The cross between floxed *Dyrk1a* and CMV-Cre on B6 background did not produce any pups heterozygous of Dyrk1a null allele (0/93 pups), but a few live pups were mosaic for floxed and null allele. Crossing male mosaic mice to wild type B6 females did not produce any pups (0/46 pups). In contrast, crossing the same male mosaic mice to wild type 129S1 females produced live pups heterozygous of *Dyrk1a* null allele (*Dyrk1a+/-,* 15/81 pups). Further backcrossing to 129S1 produced *Dyrk1a*+/- mice at Mendelian ratios.

998 Phenotyping of *Dyrk1a* +/- mice
999
1000 Mice on 129B6 F1 background were used for phenotyping. Western blots were performed with
1001 cortical tissues obtained from *Dyrk1a*+/- and wild type mice at 13 weeks of age, using standard
1002 procedures and antibodies against DYRK1A (Cell Signaling #8756, 1:1000) and α-tubulin
1003 (ThermoFisher #A11126, 1:5000, loading control). Protein levels were quantified using ImageJ.
1004 For each sample, DYRK1A protein level was normalized to that of α-tubulin.
1005
1006 Activity of mice was analyzed at 10 to 12 weeks of age with an open field apparatus where a
1007 single mouse was allowed to explore freely for 30 min and recorded by video. Activity was
1008 analyzed using idTracker (Perez-Escudero et al., Nature Methods, 2014). Distance travelled per
1009 5 min and time spent in the center square were quantified.
1010
1011 For brain weight and morphology, mice were euthanized at 12 weeks of age and perfused with
1012 4% paraformaldehyde. Whole brains were dissected and weighted. Brain sections were cut at 70
1013 µm thickness and stained with H&E method.
1014
1015 *Dyrk1a* knockout mESC
1016
1017 C57Bl6/J mESC (line #49) were grown on irradiated mouse embryo fibroblasts in 2i/FCS/LIF
1018 media (Czechanski et al. 2014). Exon 3 of *Dyrk1a* (Dyrk1a-202, ENMUST00000119878) was
1019 deleted in ESC using CRISPR/Cas9. Briefly, oligos encoding guide RNAs targeting intron 2 and
1020 intron 3 of murine *Dyrk1a* were cloned into plasmid pX459 v2.0 (Addgene plasmid # 62988) and
1021 sequence verified. Plasmids encoding *Dyrk1a* sgRNAs were transfected into mouse ESC using
1022 Lipofectamine 3000 (Life/Thermo) at a ratio of 1 ug total plasmid per 200,000 cells. After 24 hours,
1023 cells were transferred to irradiated DR4 puromycin-resistant mouse embryo fibroblasts and
1024 transfected cells were selected for 40 hours with 1 ug/ml puromycin. Cells were then removed
1025 from puromycin selection and cultured for 1 week, then individual colonies were picked into 96
1026 well plates. Clones were genotyped by PCR with primers Dyrk1a_For (5'-
1027 CATTCCATGCTGCTGGCCTTC-3') and Dyrk1a_Rev: 5'-GCCAGCAGCATGGAATGAGAAC-3')
1028 and analyzed by gel electrophoresis. Clones completely missing a wildtype band (1712 bp) were
1029 further expanded and re-genotyped for confirmation of loss of exon 3.
1030
1031
1032
1033
1034
1035
1036
1037
1038
1039
1040
1041

References

1 Ghosh, S., Nehme, R. & Barrett, L. E. Greater genetic diversity is needed in human pluripotent stem cell models. *Nat Commun* **13**, 7301, doi:10.1038/s41467-022-34940-z (2022).

2 Chandler, C. H., Chari, S. & Dworkin, I. Does your gene need a background check? How genetic background impacts the analysis of mutations, genes, and evolution. *Trends Genet* **29**, 358-366, doi:10.1016/j.tig.2013.01.009 (2013).

3 Erickson, R. P. Mouse models of human genetic disease: which mouse is more like a man? *Bioessays* **18**, 993-998, doi:10.1002/bies.950181209 (1996).

4 Riordan, J. D. & Nadeau, J. H. From Peas to Disease: Modifier Genes, Network Resilience, and the Genetics of Health. *Am J Hum Genet* **101**, 177-191, doi:10.1016/j.ajhg.2017.06.004 (2017).

5 Keller, M. P. *et al.* Genetic Drivers of Pancreatic Islet Function. *Genetics* **209**, 335-356, doi:10.1534/genetics.118.300864 (2018).

6 Molenhuis, R. T. *et al.* Modeling the quantitative nature of neurodevelopmental disorders using Collaborative Cross mice. *Mol Autism* **9**, 63, doi:10.1186/s13229-018-0252-2 (2018).

7 Neuner, S. M., Heuer, S. E., Huentelman, M. J., O'Connell, K. M. S. & Kaczorowski, C. C. Harnessing Genetic Complexity to Enhance Translatability of Alzheimer's Disease Mouse Models: A Path toward Precision Medicine. *Neuron* **101**, 399-411 e395, doi:10.1016/j.neuron.2018.11.040 (2019).

8 Li, H. & Auwerx, J. Mouse Systems Genetics as a Prelude to Precision Medicine. *Trends Genet* **36**, 259-272, doi:10.1016/j.tig.2020.01.004 (2020).

9 Moore, S. J., Murphy, G. G. & Cazares, V. A. Turning strains into strengths for understanding psychiatric disorders. *Mol Psychiatry* **25**, 3164-3177, doi:10.1038/s41380-020-0772-y (2020).

10 Onos, K. D. *et al.* Enhancing face validity of mouse models of Alzheimer's disease with natural genetic variation. *PLoS Genet* **15**, e1008155, doi:10.1371/journal.pgen.1008155 (2019).

11 Sittig, L. J. *et al.* Genetic Background Limits Generalizability of Genotype-Phenotype Relationships. *Neuron* **91**, 1253-1259, doi:10.1016/j.neuron.2016.08.013 (2016).

12 Swanzey, E., O'Connor, C. & Reinholdt, L. G. Mouse Genetic Reference Populations: Cellular Platforms for Integrative Systems Genetics. *Trends Genet* **37**, 251-265, doi:10.1016/j.tig.2020.09.007 (2021).

13 Czechanski, A. *et al.* Derivation and characterization of mouse embryonic stem cells from permissive and nonpermissive strains. *Nat Protoc* **9**, 559-574, doi:10.1038/nprot.2014.030 (2014).

14 Skelly, D. A. *et al.* Mapping the Effects of Genetic Variation on Chromatin State and Gene Expression Reveals Loci That Control Ground State Pluripotency. *Cell Stem Cell* **27**, 459-469 e458, doi:10.1016/j.stem.2020.07.005 (2020).

15 Garbutt, T. A. *et al.* Permissiveness to form pluripotent stem cells may be an evolutionarily derived characteristic in Mus musculus. *Sci Rep* **8**, 14706, doi:10.1038/s41598-018-32116-8 (2018).

16 Swanzey, E., McNamara, T. F., Apostolou, E., Tahiliani, M. & Stadtfeld, M. A Susceptibility Locus on Chromosome 13 Profoundly Impacts the Stability of Genomic Imprinting in Mouse Pluripotent Stem Cells. *Cell Rep* **30**, 3597-3604 e3593, doi:10.1016/j.celrep.2020.02.073 (2020).

17 Ortmann, D. *et al.* Naive Pluripotent Stem Cells Exhibit Phenotypic Variability that Is Driven by Genetic Variation. *Cell Stem Cell* **27**, 470-481 e476, doi:10.1016/j.stem.2020.07.019 (2020).
18 Fernando, M. B., Ahfeldt, T. & Brennand, K. J. Modeling the complex genetic architectures of brain disease. *Nat Genet* **52**, 363-369, doi:10.1038/s41588-020-0596-3 (2020).
19 Tejedor, F. *et al.* minibrain: a new protein kinase family involved in postembryonic neurogenesis in Drosophila. *Neuron* **14**, 287-301, doi:10.1016/0896-6273(95)90286-4 (1995).
20 Branca, C. *et al.* Dyrk1 inhibition improves Alzheimer's disease-like pathology. *Aging Cell* **16**, 1146-1154, doi:10.1111/acel.12648 (2017).
21 Feki, A. & Hibaoui, Y. DYRK1A Protein, A Promising Therapeutic Target to Improve Cognitive Deficits in Down Syndrome. *Brain Sci* **8**, doi:10.3390/brainsci8100187 (2018).
22 Fernandez-Martinez, P., Zahonero, C. & Sanchez-Gomez, P. DYRK1A: the double-edged kinase as a protagonist in cell growth and tumorigenesis. *Mol Cell Oncol* **2**, e970048, doi:10.4161/23723548.2014.970048 (2015).
23 Dang, T. *et al.* Autism-associated Dyrk1a truncation mutants impair neuronal dendritic and spine growth and interfere with postnatal cortical development. *Mol Psychiatry* **23**, 747-758, doi:10.1038/mp.2016.253 (2018).
24 Earl, R. K. *et al.* Clinical phenotype of ASD-associated DYRK1A haploinsufficiency. *Mol Autism* **8**, 54, doi:10.1186/s13229-017-0173-5 (2017).
25 Arbones, M. L., Thomazeau, A., Nakano-Kobayashi, A., Hagiwara, M. & Delabar, J. M. DYRK1A and cognition: A lifelong relationship. *Pharmacol Ther* **194**, 199-221, doi:10.1016/j.pharmthera.2018.09.010 (2019).
26 Gaspard, N. *et al.* Generation of cortical neurons from mouse embryonic stem cells. *Nat Protoc* **4**, 1454-1463, doi:10.1038/nprot.2009.157 (2009).
27 Bibel, M. *et al.* Differentiation of mouse embryonic stem cells into a defined neuronal lineage. *Nat Neurosci* **7**, 1003-1009, doi:10.1038/nn1301 (2004).
28 Bian, J., Zheng, J., Li, S., Luo, L. & Ding, F. Sequential Differentiation of Embryonic Stem Cells into Neural Epithelial-Like Stem Cells and Oligodendrocyte Progenitor Cells. *PLoS One* **11**, e0155227, doi:10.1371/journal.pone.0155227 (2016).
29 Pollard, S. M., Wallbank, R., Tomlinson, S., Grotewold, L. & Smith, A. Fibroblast growth factor induces a neural stem cell phenotype in foetal forebrain progenitors and during embryonic stem cell differentiation. *Mol Cell Neurosci* **38**, 393-403, doi:10.1016/j.mcn.2008.03.012 (2008).
30 Ying, Q. L. & Smith, A. G. Defined conditions for neural commitment and differentiation. *Methods Enzymol* **365**, 327-341, doi:10.1016/s0076-6879(03)65023-8 (2003).
31 Shi, Y., Kirwan, P. & Livesey, F. J. Directed differentiation of human pluripotent stem cells to cerebral cortex neurons and neural networks. *Nat Protoc* **7**, 1836-1846, doi:10.1038/nprot.2012.116 (2012).
32 Miyabayashi, T., Yamamoto, M., Sato, A., Sakano, S. & Takahashi, Y. Indole derivatives sustain embryonic stem cell self-renewal in long-term culture. *Biosci Biotechnol Biochem* **72**, 1242-1248, doi:10.1271/bbb.70717 (2008).
33 Hasegawa, K. *et al.* Wnt signaling orchestration with a small molecule DYRK inhibitor provides long-term xeno-free human pluripotent cell expansion. *Stem Cells Transl Med* **1**, 18-28, doi:10.5966/sctm.2011-0033 (2012).
34 Monteiro, M. B. *et al.* A High-Throughput Screen Identifies DYRK1A Inhibitor ID-8 that Stimulates Human Kidney Tubular Epithelial Cell Proliferation. *J Am Soc Nephrol* **29**, 2820-2833, doi:10.1681/ASN.2018040392 (2018).
35 Bellmaine, S. F. *et al.* Inhibition of DYRK1A disrupts neural lineage specificationin human pluripotent stem cells. *Elife* **6**, doi:10.7554/eLife.24502 (2017).

36 Aydin, S. *et al.* Genetic dissection of the pluripotent proteome through multi-omics data integration. *Cell Genom* **3**, 100283, doi:10.1016/j.xgen.2023.100283 (2023).
37 Ying, Q. L. *et al.* The ground state of embryonic stem cell self-renewal. *Nature* **453**, 519-523, doi:10.1038/nature06968 (2008).
38 Nichols, J., Silva, J., Roode, M. & Smith, A. Suppression of Erk signalling promotes ground state pluripotency in the mouse embryo. *Development* **136**, 3215-3222, doi:10.1242/dev.038893 (2009).
39 Pantazis, C. B. *et al.* A reference human induced pluripotent stem cell line for large-scale collaborative studies. *Cell Stem Cell* **29**, 1685-1702 e1622, doi:10.1016/j.stem.2022.11.004 (2022).
40 Zhang, Y., Hoxha, E., Zhao, T., Zhou, X. & Alvarez-Bolado, G. Foxb1 Regulates Negatively the Proliferation of Oligodendrocyte Progenitors. *Front Neuroanat* **11**, 53, doi:10.3389/fnana.2017.00053 (2017).
41 van de Leemput, J. *et al.* CORTECON: a temporal transcriptome analysis of in vitro human cerebral cortex development from human embryonic stem cells. *Neuron* **83**, 51-68, doi:10.1016/j.neuron.2014.05.013 (2014).
42 Alexander, T., Nolte, C. & Krumlauf, R. Hox genes and segmentation of the hindbrain and axial skeleton. *Annu Rev Cell Dev Biol* **25**, 431-456, doi:10.1146/annurev.cellbio.042308.113423 (2009).
43 Shimazaki, T., Shingo, T. & Weiss, S. The ciliary neurotrophic factor/leukemia inhibitory factor/gp130 receptor complex operates in the maintenance of mammalian forebrain neural stem cells. *J Neurosci* **21**, 7642-7653 (2001).
44 Desai, S. *et al.* Tissue-specific isoform switch and DNA hypomethylation of the pyruvate kinase PKM gene in human cancers. *Oncotarget* **5**, 8202-8210, doi:10.18632/oncotarget.1159 (2014).
45 Toiber, D. *et al.* Engineering DYRK1A overdosage yields Down syndrome-characteristic cortical splicing aberrations. *Neurobiol Dis* **40**, 348-359, doi:10.1016/j.nbd.2010.06.011 (2010).
46 Shi, J. *et al.* Increased dosage of Dyrk1A alters alternative splicing factor (ASF)-regulated alternative splicing of tau in Down syndrome. *J Biol Chem* **283**, 28660-28669, doi:10.1074/jbc.M802645200 (2008).
47 Alvarez, M., Estivill, X. & de la Luna, S. DYRK1A accumulates in splicing speckles through a novel targeting signal and induces speckle disassembly. *J Cell Sci* **116**, 3099-3107, doi:10.1242/jcs.00618 (2003).
48 Ding, S. *et al.* Regulation of alternative splicing of tau exon 10 by 9G8 and Dyrk1A. *Neurobiol Aging* **33**, 1389-1399, doi:10.1016/j.neurobiolaging.2010.11.021 (2012).
49 Levy, J. A., LaFlamme, C. W., Tsaprailis, G., Crynen, G. & Page, D. T. Dyrk1a Mutations Cause Undergrowth of Cortical Pyramidal Neurons via Dysregulated Growth Factor Signaling. *Biol Psychiatry* **90**, 295-306, doi:10.1016/j.biopsych.2021.01.012 (2021).
50 Togashi, H., Sakisaka, T. & Takai, Y. Cell adhesion molecules in the central nervous system. *Cell Adh Migr* **3**, 29-35, doi:10.4161/cam.3.1.6773 (2009).
51 Majer, A. *et al.* The cell type resolved mouse transcriptome in neuron-enriched brain tissues from the hippocampus and cerebellum during prion disease. *Sci Rep* **9**, 1099, doi:10.1038/s41598-018-37715-z (2019).
52 Ning, S., Pagano, J. S. & Barber, G. N. IRF7: activation, regulation, modification and function. *Genes Immun* **12**, 399-414, doi:10.1038/gene.2011.21 (2011).
53 Ozdinler, P. H. & Erzurumlu, R. S. Slit2, a branching-arborization factor for sensory axons in the Mammalian CNS. *J Neurosci* **22**, 4540-4549, doi:10.1523/JNEUROSCI.22-11-04540.2002 (2002).

54 Ori-McKenney, K. M. *et al.* Phosphorylation of beta-Tubulin by the Down Syndrome Kinase, Minibrain/DYRK1a, Regulates Microtubule Dynamics and Dendrite Morphogenesis. *Neuron* **90**, 551-563, doi:10.1016/j.neuron.2016.03.027 (2016).
55 Martinez de Lagran, M. *et al.* Dyrk1A influences neuronal morphogenesis through regulation of cytoskeletal dynamics in mammalian cortical neurons. *Cereb Cortex* **22**, 2867-2877, doi:10.1093/cercor/bhr362 (2012).
56 Cortes, D. & Pera, M. F. The genetic basis of inter-individual variation in recovery from traumatic brain injury. *NPJ Regen Med* **6**, 5, doi:10.1038/s41536-020-00114-y (2021).
57 Lisi, V. *et al.* Enhanced Neuronal Regeneration in the CAST/Ei Mouse Strain Is Linked to Expression of Differentiation Markers after Injury. *Cell Rep* **20**, 1136-1147, doi:10.1016/j.celrep.2017.07.010 (2017).
58 Quiles Del Rey, M. & Mancias, J. D. NCOA4-Mediated Ferritinophagy: A Potential Link to Neurodegeneration. *Front Neurosci* **13**, 238, doi:10.3389/fnins.2019.00238 (2019).
59 Fotaki, V. *et al.* Dyrk1A haploinsufficiency affects viability and causes developmental delay and abnormal brain morphology in mice. *Mol Cell Biol* **22**, 6636-6647, doi:10.1128/mcb.22.18.6636-6647.2002 (2002).
60 Ferron, S. R. *et al.* Regulated segregation of kinase Dyrk1A during asymmetric neural stem cell division is critical for EGFR-mediated biased signaling. *Cell Stem Cell* **7**, 367-379, doi:10.1016/j.stem.2010.06.021 (2010).
61 Benavides-Piccione, R. *et al.* Alterations in the phenotype of neocortical pyramidal cells in the Dyrk1A+/- mouse. *Neurobiol Dis* **20**, 115-122, doi:10.1016/j.nbd.2005.02.004 (2005).
62 Arque, G. *et al.* Impaired spatial learning strategies and novel object recognition in mice haploinsufficient for the dual specificity tyrosine-regulated kinase-1A (Dyrk1A). *PLoS One* **3**, e2575, doi:10.1371/journal.pone.0002575 (2008).
63 Raveau, M., Shimohata, A., Amano, K., Miyamoto, H. & Yamakawa, K. DYRK1A-haploinsufficiency in mice causes autistic-like features and febrile seizures. *Neurobiol Dis* **110**, 180-191, doi:10.1016/j.nbd.2017.12.003 (2018).
64 Murray, C. R. *et al.* Novel Causative Variants in DYRK1A, KARS, and KAT6A Associated with Intellectual Disability and Additional Phenotypic Features. *J Pediatr Genet* **6**, 77-83, doi:10.1055/s-0037-1598639 (2017).
65 Li, S. *et al.* An age-related sprouting transcriptome provides molecular control of axonal sprouting after stroke. *Nat Neurosci* **13**, 1496-1504, doi:10.1038/nn.2674 (2010).
66 Omura, T. *et al.* Robust Axonal Regeneration Occurs in the Injured CAST/Ei Mouse CNS. *Neuron* **86**, 1215-1227, doi:10.1016/j.neuron.2015.05.005 (2015).
67 Dimou, L. *et al.* Nogo-A-deficient mice reveal strain-dependent differences in axonal regeneration. *J Neurosci* **26**, 5591-5603, doi:10.1523/JNEUROSCI.1103-06.2006 (2006).
68 Tedeschi, A., Omura, T. & Costigan, M. CNS repair and axon regeneration: Using genetic variation to determine mechanisms. *Exp Neurol* **287**, 409-422, doi:10.1016/j.expneurol.2016.05.004 (2017).
69 Basso, D. M. *et al.* Basso Mouse Scale for locomotion detects differences in recovery after spinal cord injury in five common mouse strains. *J Neurotrauma* **23**, 635-659, doi:10.1089/neu.2006.23.635 (2006).
70 Ma, M., Wei, P., Wei, T., Ransohoff, R. M. & Jakeman, L. B. Enhanced axonal growth into a spinal cord contusion injury site in a strain of mouse (129X1/SvJ) with a diminished inflammatory response. *J Comp Neurol* **474**, 469-486, doi:10.1002/cne.20149 (2004).
71 Kigerl, K. A., McGaughy, V. M. & Popovich, P. G. Comparative analysis of lesion development and intraspinal inflammation in four strains of mice following spinal contusion injury. *J Comp Neurol* **494**, 578-594, doi:10.1002/cne.20827 (2006).
72 Panina, Y., Germond, A., Masui, S. & Watanabe, T. M. Validation of Common Housekeeping Genes as Reference for qPCR Gene Expression Analysis During iPS Reprogramming Process. *Sci Rep* **8**, 8716, doi:10.1038/s41598-018-26707-8 (2018).

1240 73 Roy, J. G., McElhaney, J. E. & Verschoor, C. P. Reliable reference genes for the
1241 quantification of mRNA in human T-cells and PBMCs stimulated with live influenza virus.
1242 *BMC Immunol* **21**, 4, doi:10.1186/s12865-020-0334-8 (2020).
1243 74 Sawa, A., Khan, A. A., Hester, L. D. & Snyder, S. H. Glyceraldehyde-3-phosphate
1244 dehydrogenase: nuclear translocation participates in neuronal and nonneuronal cell
1245 death. *Proc Natl Acad Sci U S A* **94**, 11669-11674, doi:10.1073/pnas.94.21.11669 (1997).
1246 75 Tanaka, R. *et al.* Induction of glyceraldehyde-3-phosphate dehydrogenase (GAPDH)
1247 expression in rat brain after focal ischemia/reperfusion. *J Cereb Blood Flow Metab* **22**,
1248 280-288, doi:10.1097/00004647-200203000-00005 (2002).
1249 76 Hara, M. R., Cascio, M. B. & Sawa, A. GAPDH as a sensor of NO stress. *Biochim Biophys*
1250 *Acta* **1762**, 502-509, doi:10.1016/j.bbadis.2006.01.012 (2006).
1251 77 Lee, F. H. *et al.* Disrupting GluA2-GAPDH Interaction Affects Axon and Dendrite
1252 Development. *Sci Rep* **6**, 30458, doi:10.1038/srep30458 (2016).
1253 78 Halladay, A. K. *et al.* Sex and gender differences in autism spectrum disorder:
1254 summarizing evidence gaps and identifying emerging areas of priority. *Mol Autism* **6**, 36,
1255 doi:10.1186/s13229-015-0019-y (2015).
1256 79 Meissner, L. E. *et al.* DYRK1A pathogenic variants in two patients with syndromic
1257 intellectual disability and a review of the literature. *Mol Genet Genomic Med* **8**, e1544,
1258 doi:10.1002/mgg3.1544 (2020).
1259 80 Chesler, E. J. *et al.* The Collaborative Cross at Oak Ridge National Laboratory: developing
1260 a powerful resource for systems genetics. *Mamm Genome* **19**, 382-389,
1261 doi:10.1007/s00335-008-9135-8 (2008).
1262 81 Andersson-Rolf, A. *et al.* One-step generation of conditional and reversible gene
1263 knockouts. *Nat Methods* **14**, 287-289, doi:10.1038/nmeth.4156 (2017).
1264 82 Wei, Z., Zhang, W., Fang, H., Li, Y. & Wang, X. esATAC: an easy-to-use systematic
1265 pipeline for ATAC-seq data analysis. *Bioinformatics* **34**, 2664-2665,
1266 doi:10.1093/bioinformatics/bty141 (2018).
1267 83 Robinson, M. D., McCarthy, D. J. & Smyth, G. K. edgeR: a Bioconductor package for
1268 differential expression analysis of digital gene expression data. *Bioinformatics* **26**, 139-
1269 140, doi:10.1093/bioinformatics/btp616 (2010).
1270 84 TW, H. B. & Girke, T. systemPipeR: NGS workflow and report generation environment.
1271 *BMC Bioinformatics* **17**, 388, doi:10.1186/s12859-016-1241-0 (2016).
1272 85 Ritchie, M. E. *et al.* limma powers differential expression analyses for RNA-sequencing
1273 and microarray studies. *Nucleic Acids Res* **43**, e47, doi:10.1093/nar/gkv007 (2015).
1274 86 topGO: Enrichment Analysis for Gene Ontology. R package version 2.42.0. v. version
1275 2.42.0. (2020).
1276 87 GO.db: A set of annotation maps describing the entire Gene Ontology v. R package
1277 version 3.8.2. (2019).
1278 88 Fletcher, M. N. *et al.* Master regulators of FGFR2 signalling and breast cancer risk. *Nat*
1279 *Commun* **4**, 2464, doi:10.1038/ncomms3464 (2013).
1280 89 Gu, Z., Gu, L., Eils, R., Schlesner, M. & Brors, B. circlize Implements and enhances
1281 circular visualization in R. *Bioinformatics* **30**, 2811-2812,
1282 doi:10.1093/bioinformatics/btu393 (2014).
1283 90 Vitting-Seerup, K., Porse, B. T., Sandelin, A. & Waage, J. spliceR: an R package for
1284 classification of alternative splicing and prediction of coding potential from RNA-seq data.
1285 *BMC Bioinformatics* **15**, 81, doi:10.1186/1471-2105-15-81 (2014).
1286 91 Almagro Armenteros, J. J. *et al.* SignalP 5.0 improves signal peptide predictions using
1287 deep neural networks. *Nat Biotechnol* **37**, 420-423, doi:10.1038/s41587-019-0036-z
1288 (2019).
1289 92 Finn, R. D. *et al.* The Pfam protein families database. *Nucleic Acids Res* **38**, D211-222,
1290 doi:10.1093/nar/gkp985 (2010).

93 Huber, W. *et al.* Orchestrating high-throughput genomic analysis with Bioconductor. *Nat Methods* **12**, 115-121, doi:10.1038/nmeth.3252 (2015).

94 Meszaros, B., Erdos, G. & Dosztanyi, Z. IUPred2A: context-dependent prediction of protein disorder as a function of redox state and protein binding. *Nucleic Acids Res* **46**, W329-W337, doi:10.1093/nar/gky384 (2018).

95 Vitting-Seerup, K. & Sandelin, A. IsoformSwitchAnalyzeR: analysis of changes in genome-wide patterns of alternative splicing and its functional consequences. *Bioinformatics* **35**, 4469-4471, doi:10.1093/bioinformatics/btz247 (2019).

96 Wang, L. *et al.* CPAT: Coding-Potential Assessment Tool using an alignment-free logistic regression model. *Nucleic Acids Res* **41**, e74, doi:10.1093/nar/gkt006 (2013).

Acknowledgments

This work was supported by the Jackson Laboratory. DEC was the recipient of a JAX Scholar Award. AE was a participant in the JAX Summer Student Program. A National Institutes of Health grant to LGR (U42 OD010921) supported mESC derivation and expansion. We thank Dr. Catherine Kaczorowski for providing access to MEA equipment and for review of the manuscript, and Ms. Anne Czechanski for her advice on mESC culture. Ann Wells, Harshpreet Chandock, and Annat Haber (The Jackson Laboratory) advised on computational analyses. We thank Hong Liu for designing genotyping protocols and genotyping.

Author Contributions

DEC: Conceptualization, Methodology, Validation, Formal Analysis, Investigation, Data Curation, Writing, Visualization, Supervision
ME: Investigation
ACK: Investigation
AE: Investigation
SCM: Formal Analysis, Visualization
SCA: Formal Analysis, Visualization
KC: Investigation
KMSO: Resources
LGR: Resources, Writing
MFP: Conceptualization, Methodology, Resources, Writing, Supervision. Project Administration, Funding Acquisition

Competing Interests

The authors declare no competing interests.

1333 Figure Legends

1334

1335 Figure 1. *mESC-derived NPC follow the default differentiation pathway into cortical*
1336 *neurons and cortical cerebral organoids*. a) Neurons start to develop processes one day
1337 after seeding and they become more convoluted after 7 days. b) Immunostaining for
1338 different cortical layer markers. c) Violin plot showing the percentage of mESC-derived
1339 neurons for each of the eight different mESC strains studied. d) Immunostaining for
1340 neurotransmitters and synaptic markers. e) Plot showing glutamatergic, forebrain and
1341 cortical layer markers from all the strains of mESC-derived neurons. Data are represented
1342 as mean ± SEM. f) Representative images of whole cell patch clamp neuron recordings,
1343 spontaneous activity on the left and evoked potentials on the right. g) representative
1344 recordings of mESC-derived neurons on MEA plates. Top left is a raster plot. Top right is
1345 a representative image of synchrony within the well. Bottom left, column plot showing
1346 spike activity (Hz) among the neurons derived from all strains. Bottom right shows the
1347 synchrony index among the neurons derived from all strains. Data are represented as
1348 mean ± SEM. h) Representative images of mESC-derived organoids showing different
1349 cortical markers. i) Top panel, calcium imaging of mESC cerebral organoids. Circles show
1350 two examples of cells with changes in calcium activity. Bottom panel, plot showing the
1351 activity of the two cells in the upper panel followed through time.

1352

1353 Figure 2. *Generation of specific neuronal subtypes by molecular patterning.* a) Scheme
1354 of the differentiation protocol to generate mESC-derived MN. b) Immunostaining for MN
1355 markers. c) Plot showing the differentiation efficiency among the eight mESC strains.
1356 Data are represented as mean ± SEM. d) Whole cell patch clamp recording performed
1357 at day 8 (left) and 11 (right) of the MN differentiation. e) Representative EPSC and IPSC
1358 recordings on mESC-derived MN. f) Scheme of the differentiation protocol to generate
1359 mESC-derived GABAergic neurons (left) with a representative image of GABAergic
1360 neurons (center) and quantification of the differentiation efficiency among all mESC tested
1361 (right). g) Scheme of the differentiation protocol to generate mESC-derived dopaminergic
1362 neurons (left) with an image of dopaminergic neurons (center) and quantification of the
1363 differentiation efficiency among all mESCs tested (right).

1364

1365 Figure 3. *Genetically diverse hPSC can be differentiated into cortical and MN.* a) Scheme
1366 of the differentiation protocol to generate hPSC-derived cortical neurons. b)
1367 Immunostaining of hPSC-derived NPC and quantification of NPC markers (bottom). Data
1368 are represented as mean ± SEM. c) Cortical layer markers after 3 weeks of maturation
1369 and quantification (right). Data are represented as mean ± SEM. d) Representative raster
1370 plot of hPSC-derived cortical neurons obtained using an MEA plate after 3 weeks of
1371 maturation (left). Quantification of frequency among the 10 genetically diverse iPSCs
1372 (right). e) Scheme of the differentiation protocol to generate HPSC-derived MN. f)
1373 Representative images of hPSC-differentiated MN showing phenotype-related markers
1374 (top) and quantification efficiency among the 10 genetically diverse iPSCs (bottom). g)
1375 Representative raster plot of hPSC-derived MNs obtained using an MEA plate after 3
1376 weeks of maturation (left) and quantification of frequency among the 10 genetically
1377 diverse iPSCs (right).

1378

1379 Figure 4. *Effects of DYRK1A inhibition on mESC maintenance and lineage specification*
1380 *vary across genetically diverse mouse strains*. a) Immunofluorescence images showing
1381 immunostaining for pluripotency markers in the eight different CC founder mESC cultured
1382 in four different culture conditions for four days. b) Heatmaps showing the percentage of
1383 cells expressing the markers in the mESC as measured by HCS. c) Morphometry analysis
1384 of the mESC colonies. d) Heatmap comparing the effects of LIF vs ID-8 treatment on the
1385 overall proportion of cells expressing the analyzed markers in the eight different mESCs,
1386 determined by HCS. Red indicates decreased percentage of cells expressing the
1387 associated marker in ID-8 compared to LIF, green means higher expression. Cell lines
1388 and markers are arranged according to the overall degree of change (arrows). *,
1389 represents statistically significant differences against the control condition (LIF+2i) within
1390 the same cell line. #, represents statistically significant differences among cell lines
1391 treated with 2i+LIF and compared to the standard cell line 129. $, represents statistically
1392 significant differences among cell lines treated with 2i+ID8 and compared to the standard
1393 cell line 129. &, represents statistically significant differences among cell lines treated with
1394 LIF and compared to the standard cell line 129. %, represents statistically significant
1395 differences among cell lines treated with ID-8 and compared to the standard cell line 129
1396 where a significant difference is indicated when $p < 0.05$. Means +/- SEM are shown.
1397 Kruskal-Wallis and Dunn's test were conducted. n = 4 biological replicates.
1398
1399 Figure 5. *DYRK1A inhibition differentially blocks neural progenitor proliferation in a strain-*
1400 *dependent fashion.* a) Representative images of the B6 and WSB mESC lines
1401 differentiated into NPC in the presence of the DYRK1A inhibitor ID-8 and analyzed at day
1402 2, 5 and 8. b) Comparison between the proportion of cells expressing the indicated
1403 markers as measured by HCS in control and ID-8 treated cells after eight days of
1404 differentiation. Red indicates decreased percentage of cells expressing the associated
1405 marker in ID-8-treated cells compared to control whereas green means an increase. Cell
1406 lines and markers are arranged according to the overall degree of change (arrows) and
1407 n = 4 biological replicates. c and d) Images and plots representing the cell count of
1408 proliferating NPCs derived from six independent cell lines different from those used in b.
1409 NPCs were cultured with or without ID-8 for 5 passages. B6 showed a decreased number
1410 of cells and proliferative markers (Ki67 and MCM2) compared to its control whereas 129,
1411 AJ and, WSB were not affected. n = 4. * Statistically different from its control, $p < 0.05$.
1412 Kruskal-Wallis and Dunn's test were conducted e) Long-term proliferation assay in hPSC-
1413 derived NPC. Left, experimental design (cells were kept in proliferative conditions as
1414 neurospheres for 15 passages (2 months total); middle, cell numbers over time; right.
1415 percentage of cells in each cycle phase measured by EdU staining in WT and DYRK1A+/-
1416 . Experiment shows DYRK1A +/- NPC undergo quiescence faster than control. Two-tailed
1417 T test, n = 4, * = $p < 0.05$.
1418
1419 Figure 6. *Neural differentiation of WT and Dyrk1a-knockout mESC.* a) Representative
1420 images at day eight of NPC differentiation showing robust differentiation in 129 and WSB
1421 but B6 *Dyrk1a*-knockout. b) Quantitation of proportion of cells expressing DYRK1A (and
1422 average intensity of DYRK1A staining) and markers of neural differentiation, pluripotency,
1423 and proliferation, measured by immunostaining and high content screening in the three

strains. Kruskal-Wallis and Dunn's test were conducted. * = $p < 0.05$ compared to its own control n = 3 biological replicates.

Figure 7. *RNA-seq analysis reveals the genes associated with the impairment in neural induction in B6-derived NPCs*. a) Venn diagram of DEG for each set of comparisons. Number in red represents downregulated genes, black indicates upregulated gene. b) RTNA for the top regulons associated with differences in ID- 8 treated WSB- and B6-derived NPCs. c) Barcode plots showing two exemplary GOs differentially affected in WSB and B6 when treated with ID-8. Genes are ranked from left to right by increasing log-fold change represented by the vertical bars. The curve shows the relative local enrichment of the bars in each part of the plot. d) Consequences of isoform switch showing a lost of exons in ID-8 treated B6 neurons. e) Venn diagram showing the global isoform switch differences in B6 vs WSB neurons when treated with ID-8. f) Switch in the *Ntrk2* isoform usage when B6 is treated with ID8, upper plot shows the color-coded domains present on each exon (bars). Bar plots indicating total gene expression, isoform expression and relative isoform usage proportional to the total gene expression.

Figure 8. *Effect of DYRK1A inhibition on delays in functional maturation of neurons by mESC strain*. a) Examples of 30 second recordings of all differentiated neurons (21 and 42 days *in vitro*) in the presence or absence of ID-8. b) Plots for firing rate, number of bursts, interburst interval, synchrony, and spikes per burst. Because the neurons from different strains do not mature and survive equally, data form comparisons among the cell lines were taken at the timepoint where the highest frequency of firing (Hz) was recorded for each cell strain. Means +/- SEM are shown. Kruskal-Wallis and Dunn's test were conducted. * = $p < 0.05$ compared to its own control n = 3 biological replicates. c) Circular plot showing different electrophysiological properties during 42 DIV in the presence of ID-8.

Figure 9. *mESC derived neuronal strain differences in recovery from axon injury in vitro*. a) Illustration of the microfluidic chamber used to isolate axons from somas. Image taken from chamber manufacturer webpage. b) Representative images of B6, WSB and NZO neurons in microfluidic chambers prior to injury, post-injury in the absence of ID-8, and post-injury in the presence of ID-8. c) Heatmap for the area occupied by axons in the chamber two (axonal side) before and after injury. d) Ratio of axonal growth compared to pre-injury in both control and treated neurons. Dunnet's test was used for statistical analysis on three biological replicates. e) MDS plot showing the differences between cell lines over all three conditions. f) Barcode plots showing GO analysis of differential response to axonal injury between WSB and B6 in the absence or presence of ID-8. g) RTNA showing the top three regulons associated with the differences between WSB and B6 when axons are injured. h) Enrichment analysis and comparison of isoform switches between the differences in axonal recovery between B6 and WSB treated or not treated with ID8; i) The isoform switch in the *Ncoa4* gene. j) Axonal recovery experiment conducted on isolated primary cortical neurons from B6 and WSB postnatal day five mice. t-test for statistical analysis on three biological replicates.

1469 Figure 10. *Heterozygous deletion of Dyrk1in mice confirms straind dependent sensitivity*
1470 *observed in vitro.* a) Generation of the null allele of *Dyrk1a* using a conditional *Dyrk1a*
1471 allele and constitutively expressed *Cre*. Exons 5 and 6 of Dyrk1a, which encode part of
1472 the kinase domain, are flanked by loxP sites. The germline CMV Cre driver removes
1473 exons 5 and 6 and the Pgk-Neo selection cassette and causes a frameshift. b-i)
1474 Phenotype of *Dyrk1a* heterozygotes in B6/129 background. b) Western blot of cortical
1475 tissues from WT and Dyrk1a$^{+/-}$ mice. α-Tub, α-tubulin. c) A Dyrk1a$^{+/-}$ mouse and a WT
1476 littermate at 12 weeks of age. d) Body weight of male mutant and control mice at 3 and
1477 12 weeks of age. e) Brains of a control and mutant at 12 weeks of age. f) Brain weights
1478 of mutant and control mice at 12 weeks of age. g) Sagittal brain sections from a WT and
1479 *Dyrk1a*$^{+/-}$ mouse at 3 months of age. Scale bar, 2 mm. h) Distance travelled by *Dyrk1a*$^{+/-}$
1480 (n = 7) and WT (n = 7) mice per five minutes in an open field apparatus. i) Percentage of
1481 time spent at the center of the arena. * $p < 0.05$, ** $p < 0.01$, *** $p < 0.001$.
1482

Supplementary Figure Legends

Fig. S1. Generation of a protocol to differentiate genetically diverse mESC into neural precursors. a) Diagram of the differentiation protocol to generate and expand NPC from mESC. b) Bright field images (left) and immunofluorescent images (right) of representative mESC differentiated into neural precursors in 8 days. NPC markers go up (Nestin), as well as forebrain markers (Pax6), pluripotency associated marker (Oct3/4) decreases completely while Sox2 remains expressed. c) Quantitative PCR for different pluripotency- and neuronal-associated markers at day 0, 2, 5 and 8 of differentiation of B6 strain mESC. Kruskal-Wallis and Dunn's test were conducted. n = 5 in triplicate. * < p 0.5, ** < 0.1, *** < 0.001 compared to day zero. Data are represented as mean ± SEM.

Fig. S2. Heatmap of the percentage of cells positive for the analyzed markers throughout eight days of differentiation in the presence of ID-8.

Fig. S3. Genetically diverse hPSC differentiated into CO. a) Scheme of the differentiation protocol to generate hPSC-derived CO. b) Top panel, calcium imaging of hPSC cerebral organoids. Circles show two examples of cells with changes in calcium activity. Bottom panel, plot showing the activity of the two cell in the upper panel followed through time. c) Representative images of 33_ 1 hPSC-derived COs at 146 days old. D Quantification of the cortical layer markers found in the hPSC-derived COs. n = 4 biological replicates.

Fig. S4. Differentiation of hPSC into dopaminergic neurons. a) Scheme for differentiation of hPSC-derived dopaminergic organoids. b) Dopaminergic (TH) and midbrain (FOXA2) markers. .

Fig. S5. Genotypic and phenotypic analysis of Dyrk1a among the eight CC founder mESC lines. a) plots depicting the number of SNPs and transcriptional variants among CC founder mESC compared to the reference genome B6. b) eQTL for both mESC and differentiated NPC show a peak in the Dyrk1a locus representing a local eQTL that can drive differences in expression specially in PWK and CAST. c) pQTL shows no differences in protein expression among all strains analyzed. d, e) Western blot shows protein abundance among mESC strains but no statistical differences.

Fig. S6. a) MDS plot comparing B6- and WSB-derived neurons treated or not with ID-8. It shows the distance between the groups and similarities in gene expression from RNA-seq samples. b) Venn diagram of DE genes for each set of comparisons. Number in red represents downregulated genes, black indicates upregulated genes in B6 compared to WSB. c) Exemplary barcode plots for differentially regulated gene sets. Conditions compared are indicated on both sides of the barcodes. d) RTNA for the top TFs associated with differences in ID-8 treated WSB- and B6-derived neurons. e) Alternative splicing analysis showing the change in alternative transcript start site (ATSS), alternative transcript termination site (ATTS), and alternative donor and acceptor sites (A5, A3) when B6 and WSB neurons are treated with ID8. f) Isoform switch for Slit2 in B6-derived neurons when treated with ID-8.

1528 Fig. S7. Comparative transcriptomic analysis across all datasets. a) Venn diagram
1529 showing the numbers of differentially expressed genes, strain-wise and treatment-wise;
1530 b) Consequences of switch analysis between the B6 and WSB strains; c) Relative
1531 expression of *Gapdh* in both strains. Two-tailed T test, n = 38, *** = $p < 0.001$; D) Bar
1532 code plots showing overall differences between the two strains in control and when
1533 treated with ID-8.
1534
1535

FIGURE 1

A

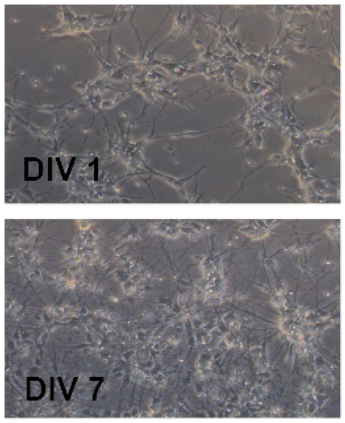

B

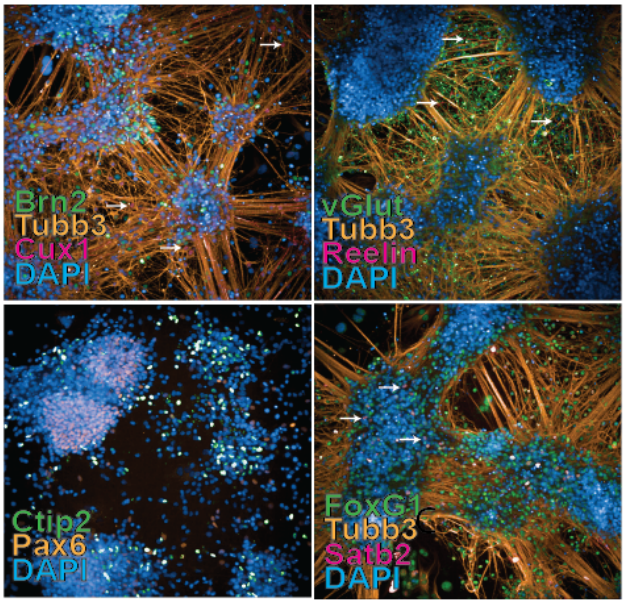

C

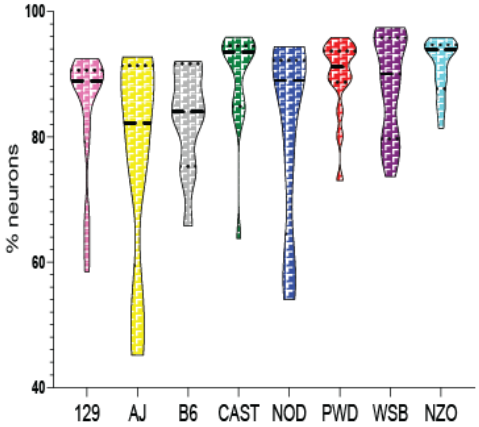

D

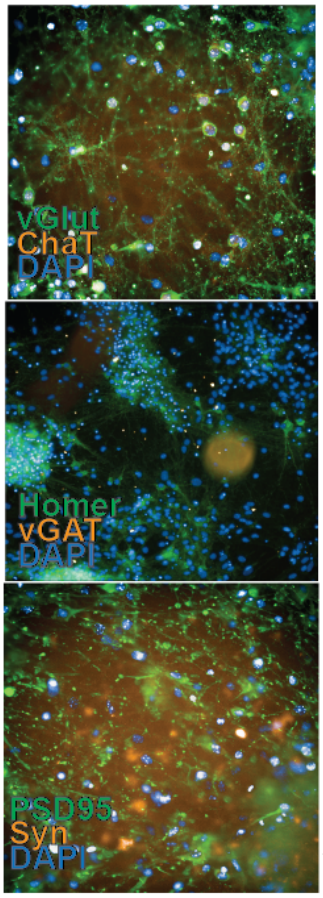

E

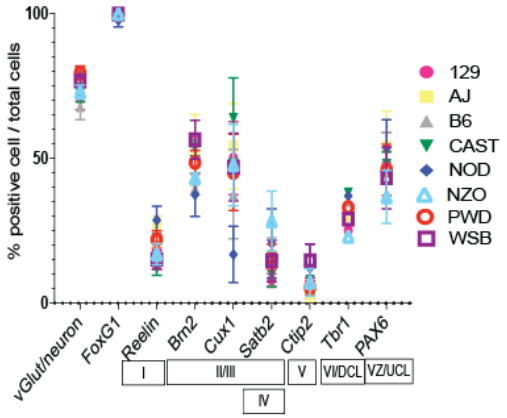

F

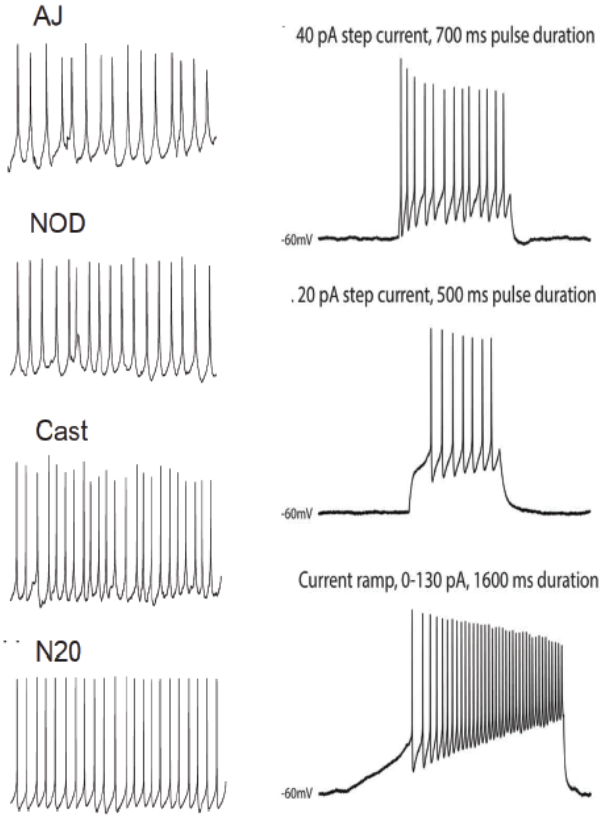

G

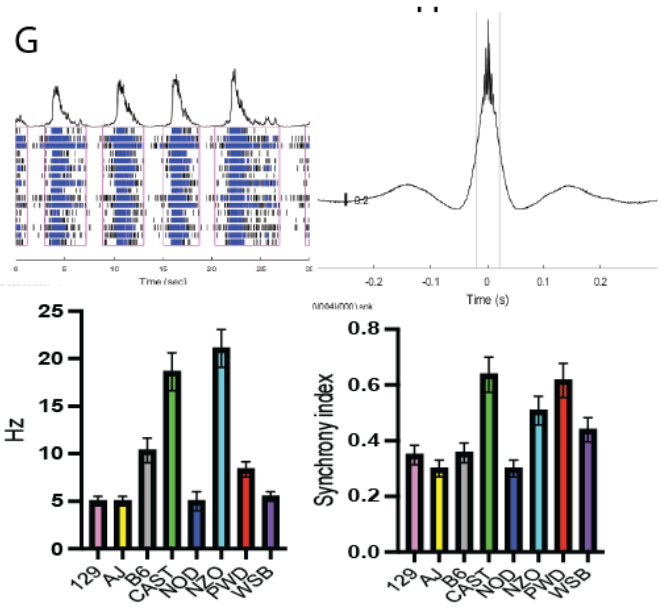

H

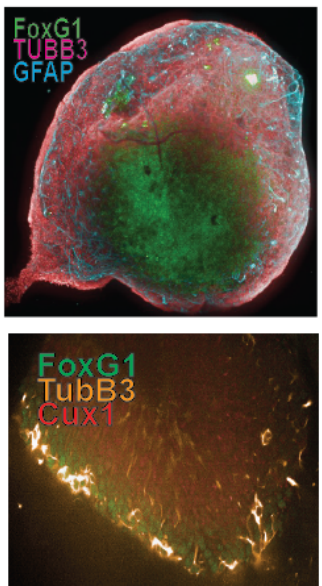

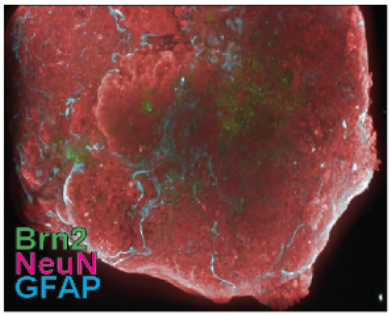

I

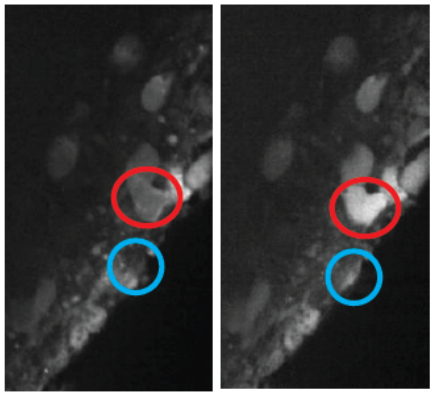

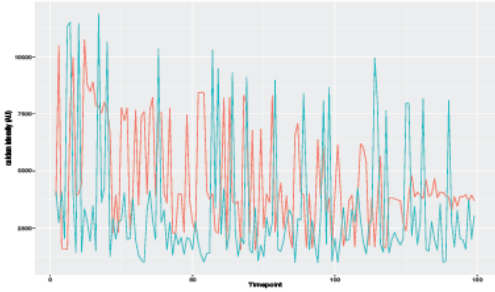

FIGURE 2

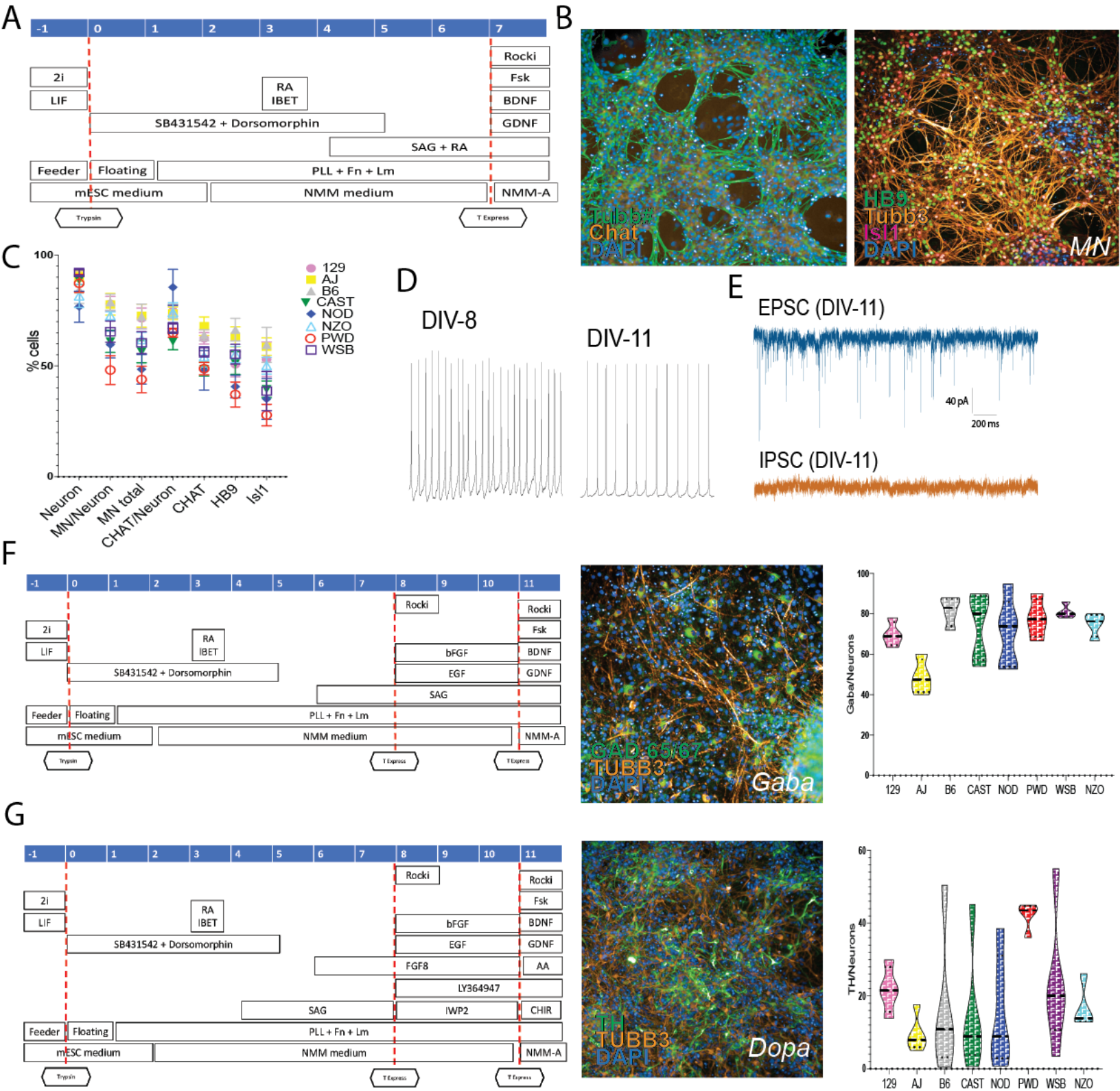
A
-1
0
1
2
3
4
5
6
7
Rocki
Fsk
BDNF
GDNF
2i
LIF
RA
IBET
SB431542 + Dorsomorphin
SAG + RA
Feeder
Floating
PLL + Fn + Lm
mESC medium
NMM medium
NMM-A
Trypsin
T Express
B
Tubb3
Chat
DAPI
HB9
Tubb3
Isl1
DAPI
MN
C
100
50
0
% cells
129
AJ
B6
CAST
NOD
NZO
PWD
WSB
Neuron
MN/Neuron
MN total
CHAT/Neuron
CHAT
HB9
Isl1
D
DIV-8
DIV-11
E
EPSC (DIV-11)
40 pA
200 ms
IPSC (DIV-11)
F
-1
0
1
2
3
4
5
6
7
8
9
10
11
Rocki
Rocki
Fsk
2i
LIF
RA
IBET
bFGF
BDNF
SB431542 + Dorsomorphin
EGF
GDNF
SAG
Feeder
Floating
PLL + Fn + Lm
mESC medium
NMM medium
NMM-A
Trypsin
T Express
T Express
GAD 65/67
TUBB3
DAPI
Gaba
100
80
60
40
20
0
Gaba/Neurons
129
AJ
B6
CAST
NOD
PWD
WSB
NZO
G
-1
0
1
2
3
4
5
6
7
8
9
10
11
Rocki
Rocki
Fsk
2i
LIF
RA
IBET
bFGF
BDNF
SB431542 + Dorsomorphin
EGF
GDNF
FGF8
AA
LY364947
SAG
IWP2
CHIR
Feeder
Floating
PLL + Fn + Lm
mESC medium
NMM medium
NMM-A
Trypsin
T Express
T Express
TH
TUBB3
DAPI
Dopa
60
40
20
0
TH/Neurons
129
AJ
B6
CAST
NOD
PWD
WSB
NZO

FIGURE 3

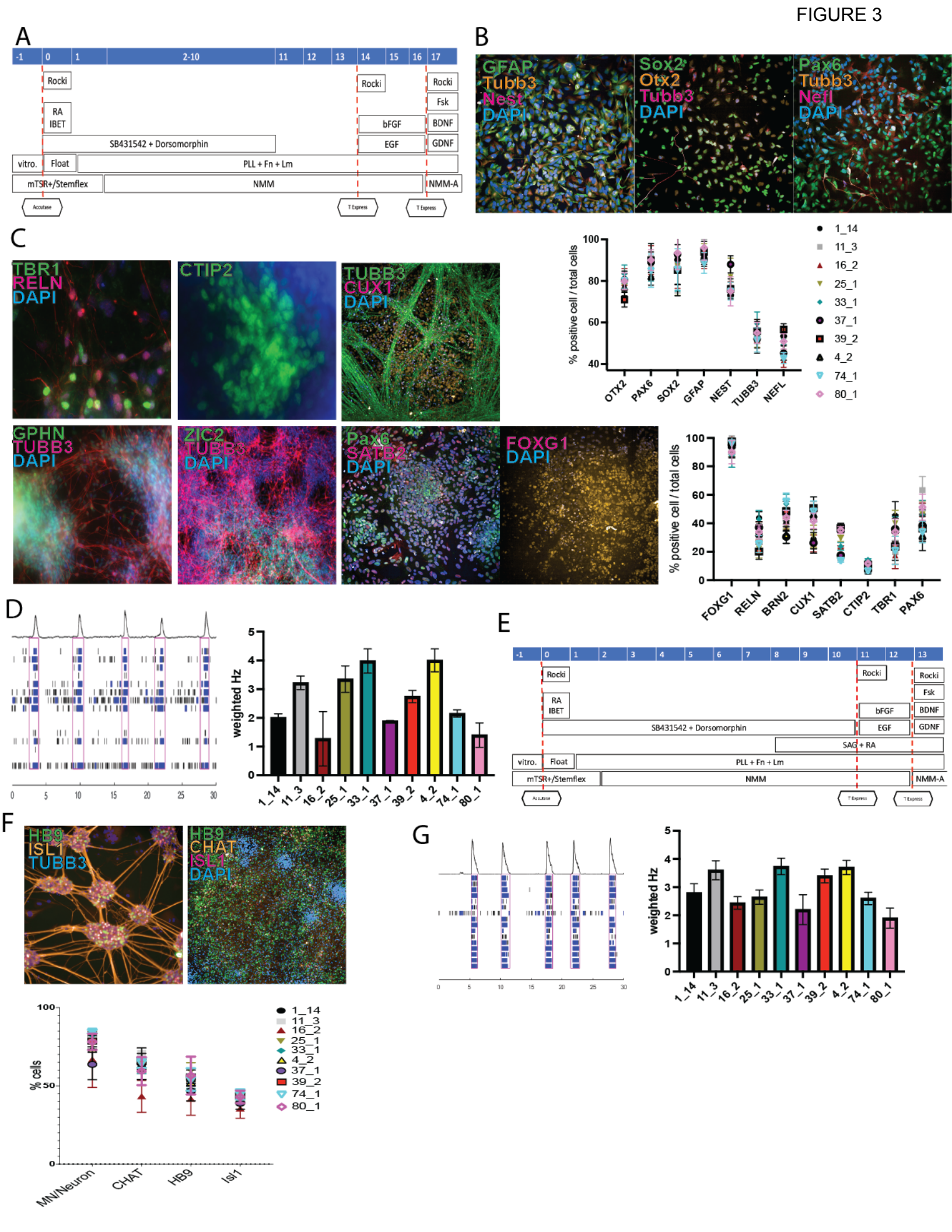
A
-1
0
1
2-10
11
12
13
14
15
16
17
Rocki
Rocki
Rocki
Fsk
RA
IBET
bFGF
BDNF
SB431542 + Dorsomorphin
EGF
GDNF
vitro.
Float
PLL + Fn + Lm
mTSR+/Stemflex
NMM
NMM-A
Accutase
T Express
T Express
B
GFAP
Tubb3
Nest
DAPI
Sox2
Otx2
Tubb3
DAPI
Pax6
Tubb3
Nefl
DAPI
C
TBR1
RELN
DAPI
CTIP2
TUBB3
CUX1
DAPI
% positive cell / total cells
OTX2
PAX6
SOX2
GFAP
NEST
TUBB3
NEFL
1_14
11_3
16_2
25_1
33_1
37_1
39_2
4_2
74_1
80_1
GPHN
TUBB3
DAPI
ZIC2
TUBB3
DAPI
Pax6
SATB2
DAPI
FOXG1
DAPI
% positive cell / total cells
FOXG1
RELN
BRN2
CUX1
SATB2
CTIP2
TBR1
PAX6
D
weighted Hz
1_14
11_3
16_2
25_1
33_1
37_1
39_2
4_2
74_1
80_1
E
-1
0
1
2
3
4
5
6
7
8
9
10
11
12
13
Rocki
Rocki
Rocki
Fsk
RA
IBET
bFGF
BDNF
SB431542 + Dorsomorphin
EGF
GDNF
SAG + RA
vitro.
Float
PLL + Fn + Lm
mTSR+/Stemflex
NMM
NMM-A
Accutase
T Express
T Express
F
HB9
ISL1
TUBB3
HB9
CHAT
ISL1
DAPI
% cells
MN/Neuron
CHAT
HB9
Isl1
1_14
11_3
16_2
25_1
33_1
4_2
37_1
39_2
74_1
80_1
G
weighted Hz
1_14
11_3
16_2
25_1
33_1
37_1
39_2
4_2
74_1
80_1

FIGURE 4

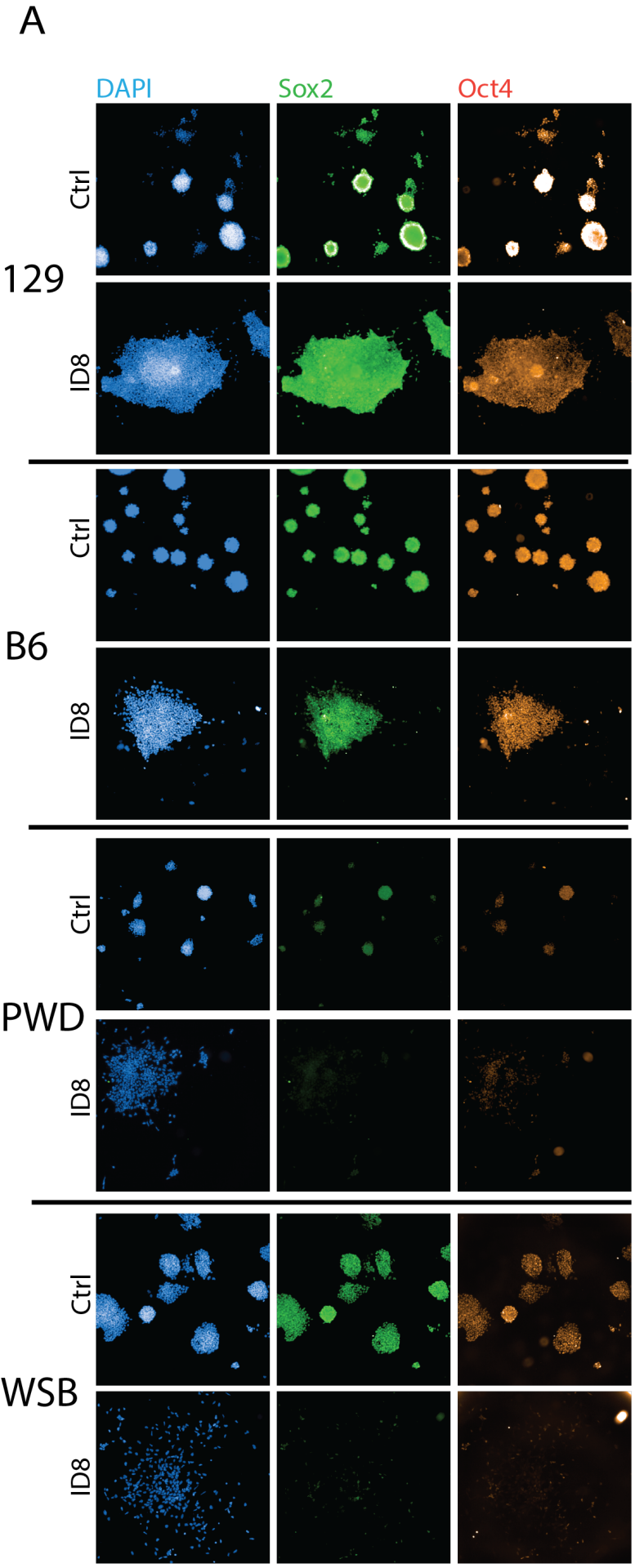
A
DAPI
Sox2
Oct4
129
B6
PWD
WSB
Ctrl
ID8

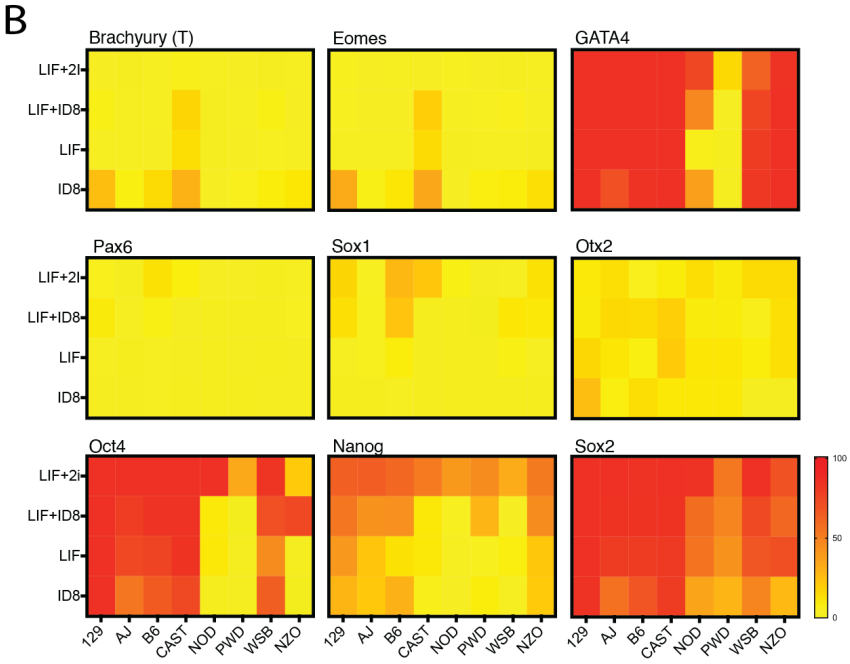
B
Brachyury (T)
Eomes
GATA4
Pax6
Sox1
Otx2
Oct4
Nanog
Sox2
LIF+2i
LIF+ID8
LIF
ID8
129
AJ
B6
CAST
NOD
PWD
WSB
NZO
100
50
0

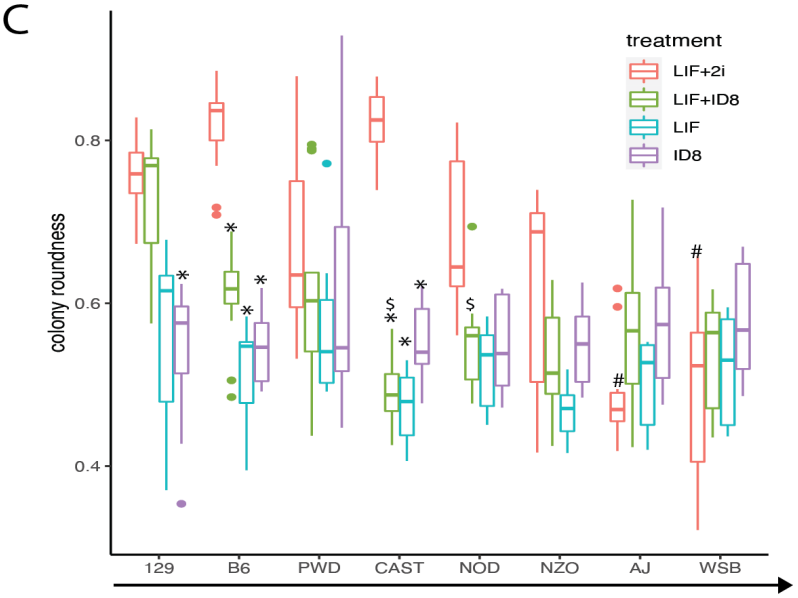
C
treatment
LIF+2i
LIF+ID8
LIF
ID8
colony roundness
0.8
0.6
0.4
129
B6
PWD
CAST
NOD
NZO
AJ
WSB

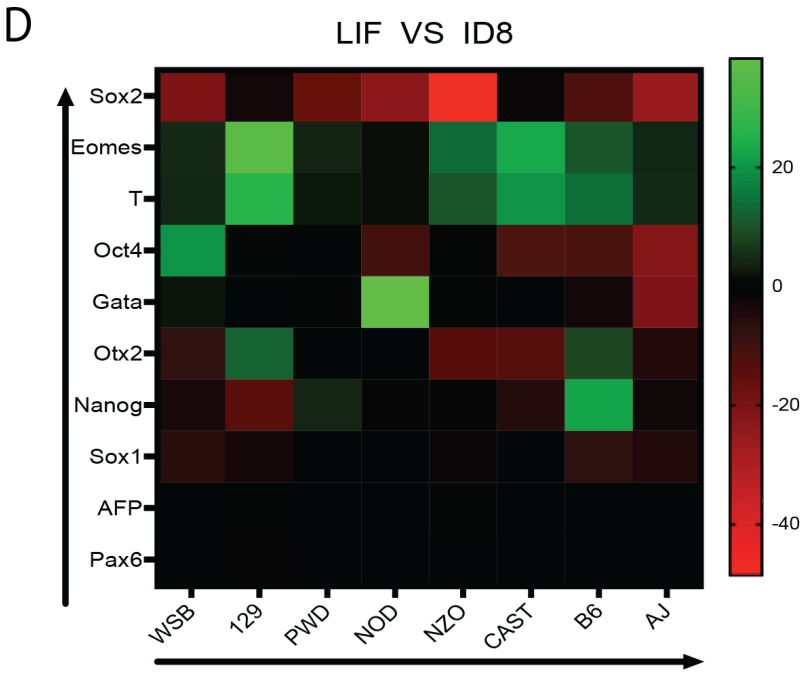
D
LIF VS ID8
Sox2
Eomes
T
Oct4
Gata
Otx2
Nanog
Sox1
AFP
Pax6
WSB
129
PWD
NOD
NZO
CAST
B6
AJ
20
0
-20
-40

FIGURE 5

A

B6 | WSB

CTRL | ID8 | CTRL | ID8 | CTRL | ID8 | CTRL | ID8

Day 2

Day 5

Day 8

Oct4 Nanog Gata4

Ki67 TubB3

B

CAST, B6, PWD, NZO, NOD, 129, AJ, WSB

Gata4, Oct4, Nanog, Eomes, T, Sox2, Ki67, Sox1, Pax6, Otx2, Tubb3

20, 10, 0, -10, -20

C

129, AJ, B6, WSB

DAPI Ki67 MCM2

Ctl

ID-8

D

cell count

10^6 cells

MCM2

Ki67

ID-8

Control

129-1, 129-2, AJ-1, AJ-2, B6-1, B6-2, WSB-1, WSB-2

E

d15

P0, P5, P10, P15

Neural progenitor formation

Neural progenitor expansion (Neurosphere Culture)

Neural precursor cell medium

Neural progenitors

d0

dissociation

neurosphere

d4

Low attachment 96-wells plate

From P_n to P_{n+1} (4 days)

2000 cells

8000 cells

16000 cells

32000 cells

Daily proliferation rate

EdU staining

% of cells/ cycle pahse

G0G1, S, G2/M

P5, P10

WT DYRK1A+/-

A

FIGURE 6

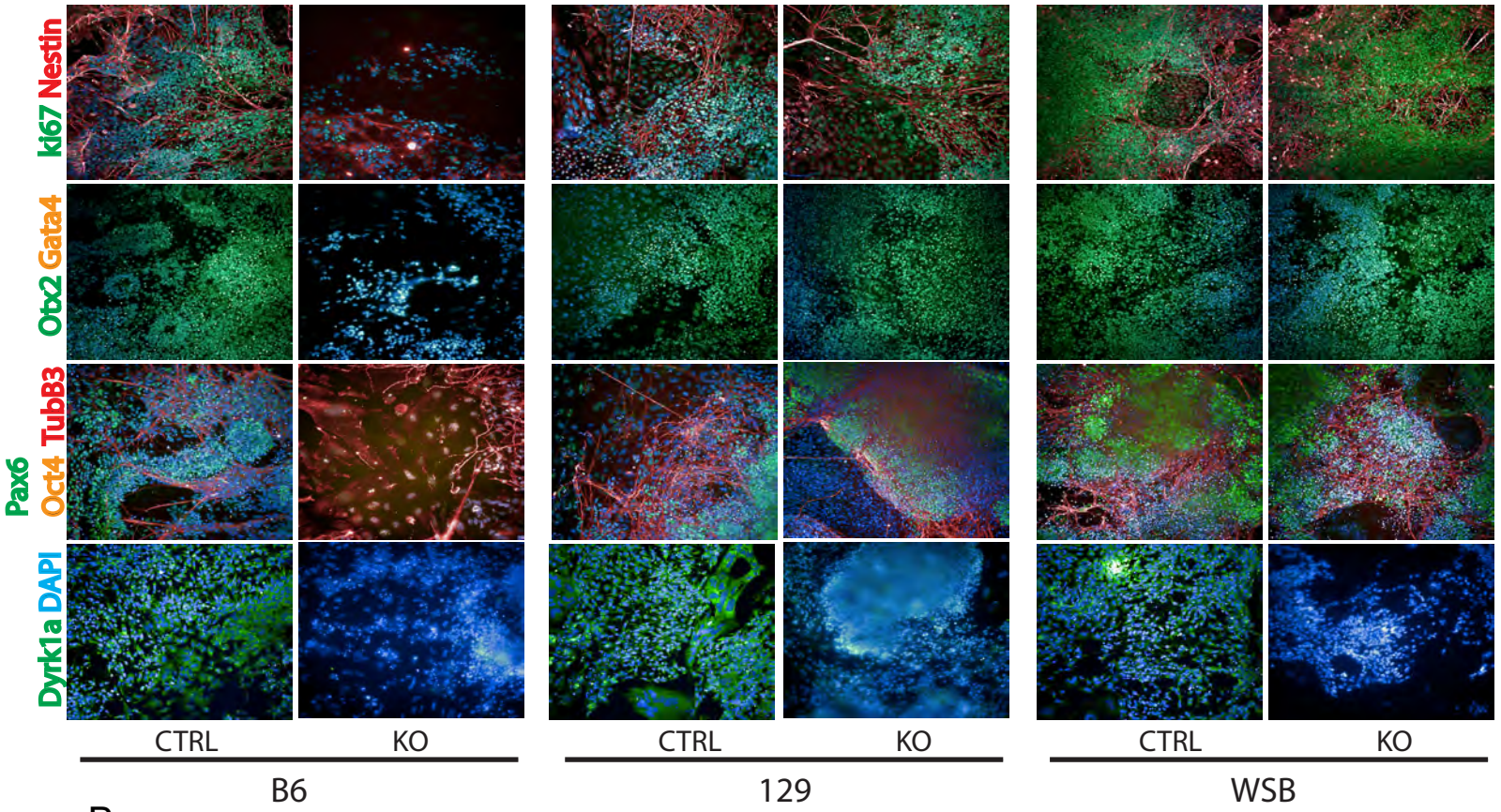
Ki67 Nestin
Otx2 Gata4
Pax6 TubB3 Oct4
Dyrk1a DAPI
CTRL
KO
CTRL
KO
CTRL
KO
B6
129
WSB

B

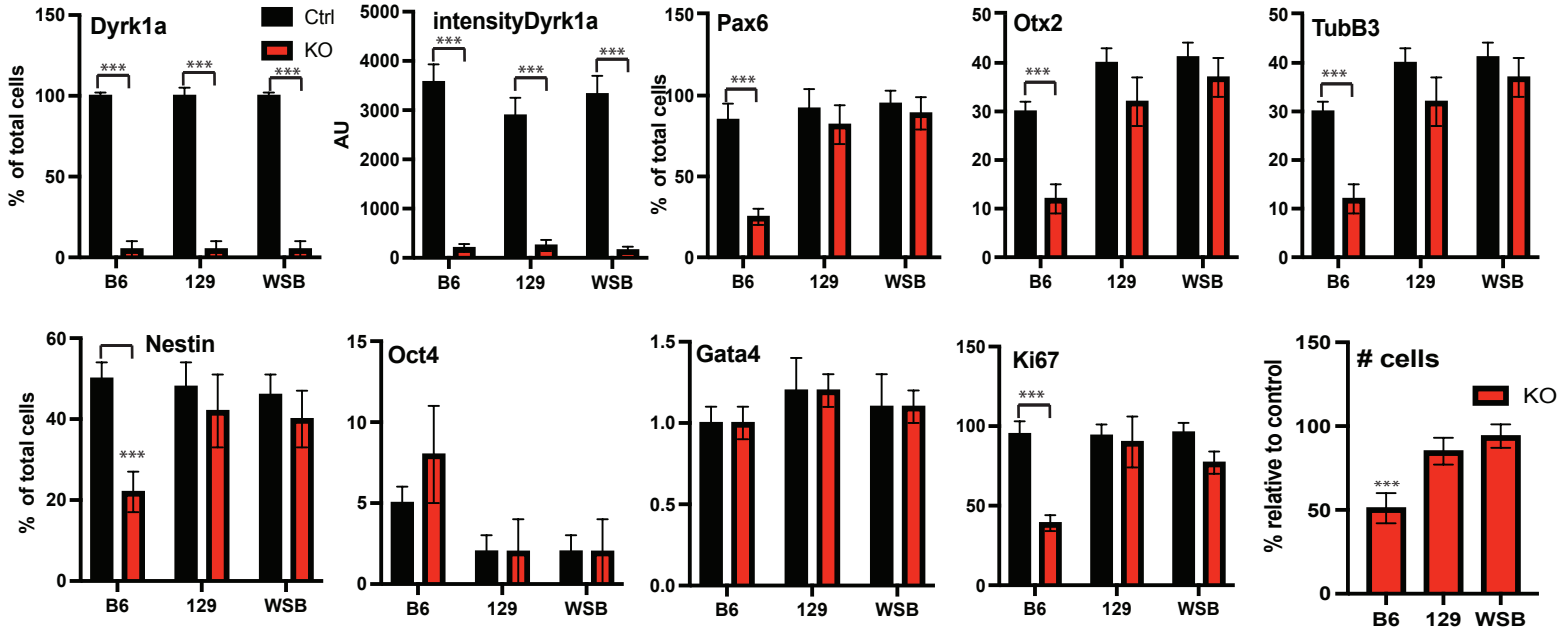
Dyrk1a
Ctrl
KO
% of total cells
intensityDyrk1a
AU
Pax6
% of total cells
Otx2
TubB3
Nestin
% of total cells
Oct4
Gata4
Ki67
cells
% relative to control
KO
B6
129
WSB
***

FIGURE 7

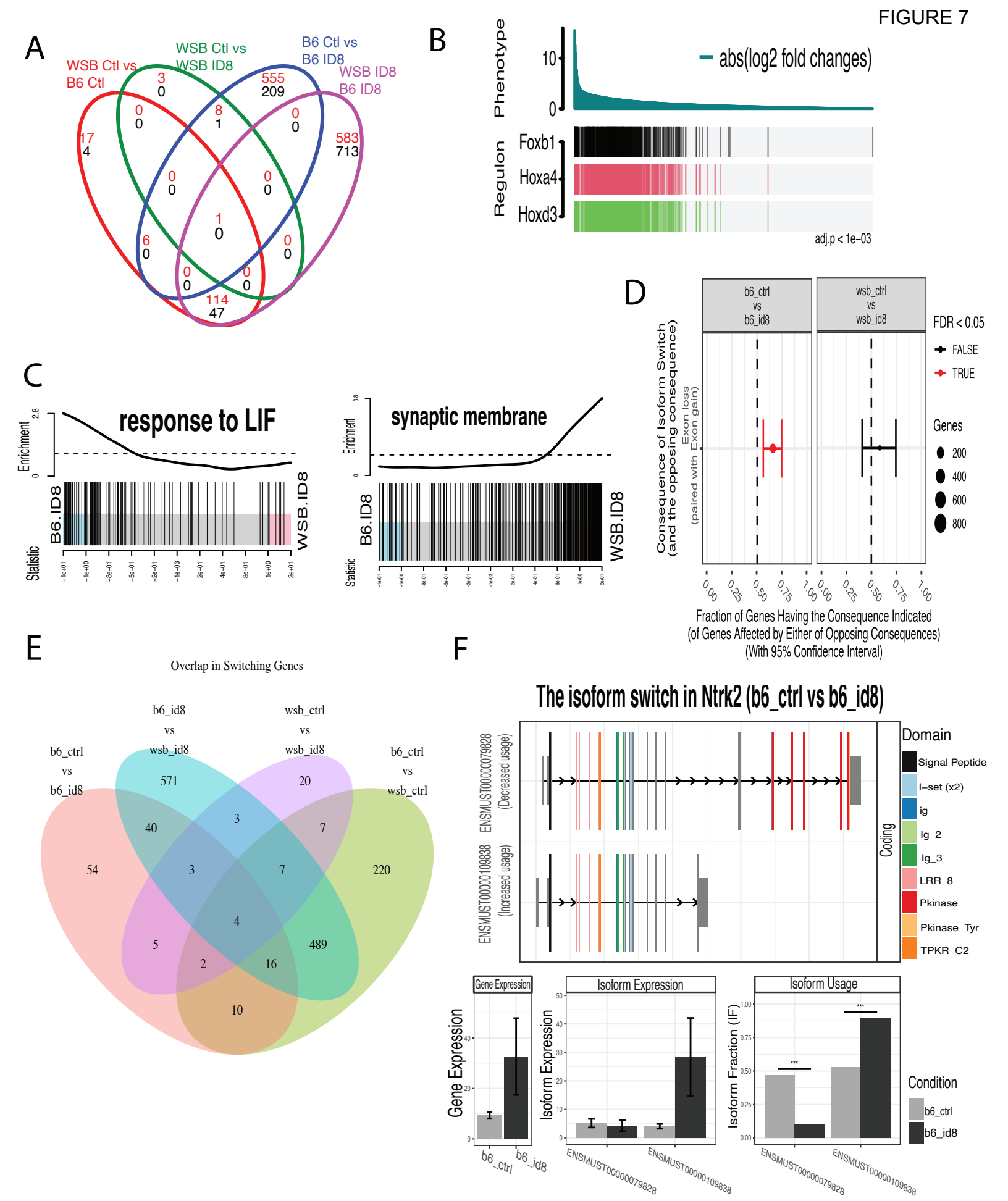
A
WSB Ctl vs B6 Ctl
WSB Ctl vs WSB ID8
B6 Ctl vs B6 ID8
WSB ID8 B6 ID8
3
0
555
209
0
0
8
1
0
0
17
4
583
713
0
0
0
0
1
0
6
0
0
0
0
0
114
47
B
Phenotype
10
0
abs(log2 fold changes)
Regulon
Foxb1
Hoxa4
Hoxd3
adj.p < 1e−03
C
response to LIF
Enrichment
2.8
0
B6.ID8
WSB.ID8
Statistic
synaptic membrane
Enrichment
3.8
0
B6.ID8
WSB.ID8
Statistic
D
b6_ctrl vs b6_id8
wsb_ctrl vs wsb_id8
FDR < 0.05
FALSE
TRUE
Genes
200
400
600
800
Consequence of Isoform Switch (and the opposing consequence)
Exon loss
(paired with Exon gain)
0.00
0.25
0.50
0.75
1.00
Fraction of Genes Having the Consequence Indicated
(of Genes Affected by Either of Opposing Consequences)
(With 95% Confidence Interval)
E
Overlap in Switching Genes
b6_ctrl vs b6_id8
b6_id8 vs wsb_id8
wsb_ctrl vs wsb_id8
b6_ctrl vs wsb_ctrl
571
20
54
40
3
7
220
3
7
4
5
489
2
16
10
F
The isoform switch in Ntrk2 (b6_ctrl vs b6_id8)
ENSMUST00000079828 (Decreased usage)
ENSMUST00000109838 (Increased usage)
Coding
Domain
Signal Peptide
I−set (x2)
ig
Ig_2
Ig_3
LRR_8
Pkinase
Pkinase_Tyr
TPKR_C2
Gene Expression
Gene Expression
b6_ctrl
b6_id8
Isoform Expression
Isoform Expression
ENSMUST00000079828
ENSMUST00000109838
Isoform Usage
Isoform Fraction (IF)
***
***
ENSMUST00000079828
ENSMUST00000109838
Condition
b6_ctrl
b6_id8

FIGURE 8

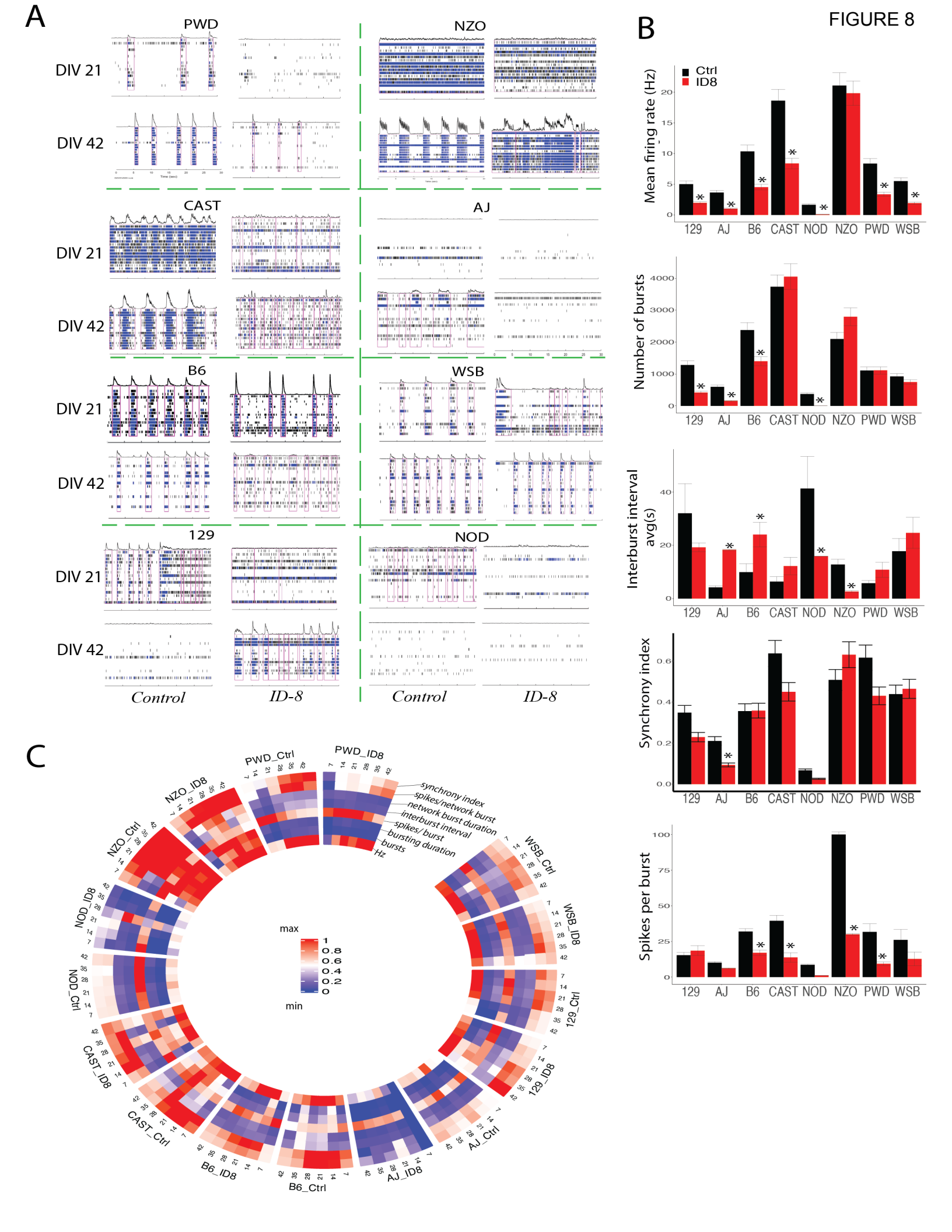
A
PWD
NZO
CAST
AJ
B6
WSB
129
NOD
DIV 21
DIV 42
Control
ID-8
B
Ctrl
ID8
Mean firing rate (Hz)
Number of bursts
Interburst interval avg(s)
Synchrony index
Spikes per burst
129
AJ
B6
CAST
NOD
NZO
PWD
WSB
C
PWD_Ctrl
PWD_ID8
NZO_ID8
NZO_Ctrl
NOD_ID8
NOD_Ctrl
CAST_ID8
CAST_Ctrl
B6_ID8
B6_Ctrl
AJ_ID8
AJ_Ctrl
129_ID8
129_Ctrl
WSB_ID8
WSB_Ctrl
synchrony index
spikes/network burst
network burst duration
interburst interval
spikes/ burst
bursting duration
bursts
Hz
max
min

FIGURE 9

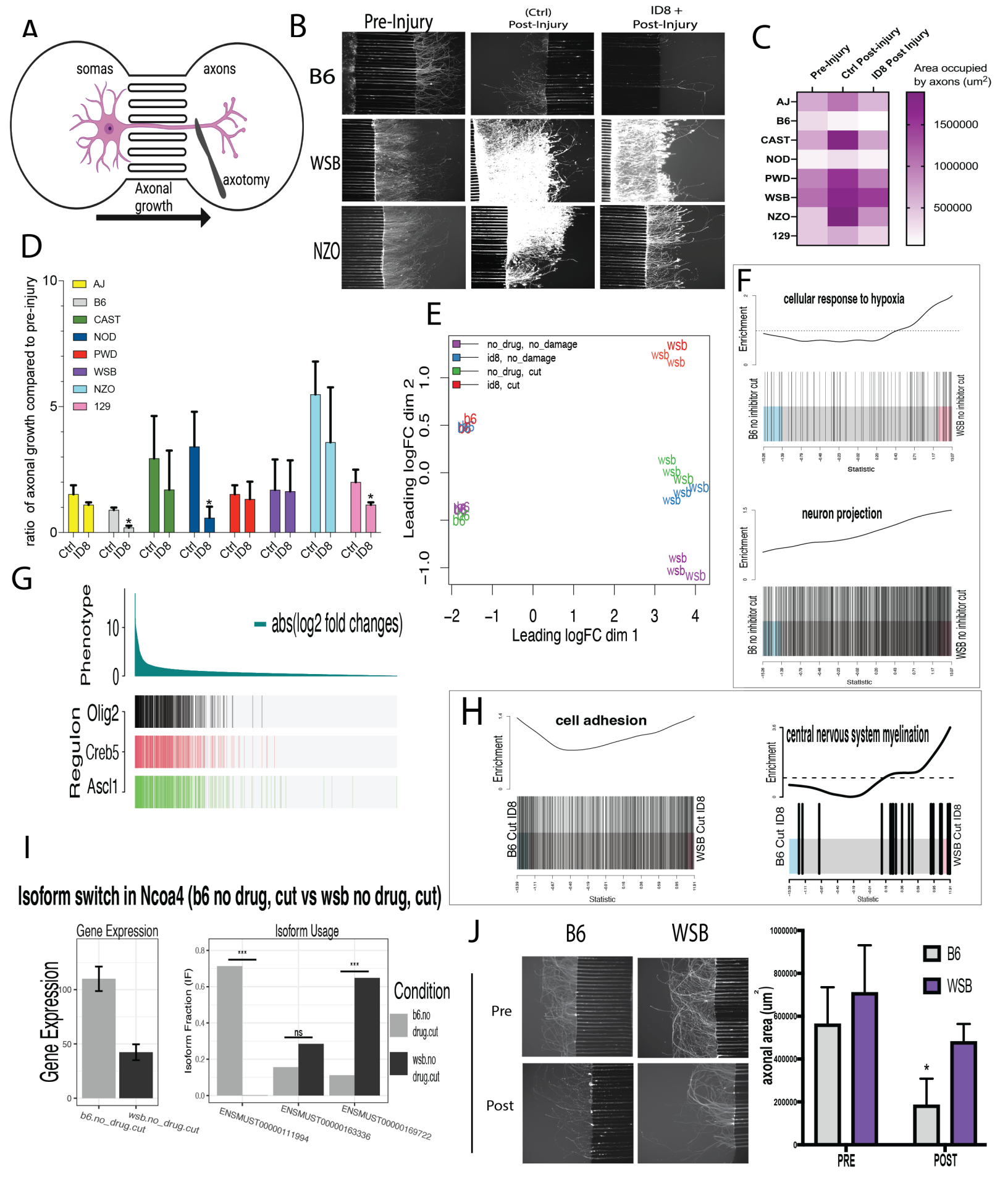
A
somas
axons
axotomy
Axonal growth
B
Pre-Injury
(Ctrl) Post-Injury
ID8 + Post-Injury
B6
WSB
NZO
C
Pre-Injury
Ctrl Post-injury
ID8 Post Injury
Area occupied by axons (um2)
AJ
B6
CAST
NOD
PWD
WSB
NZO
129
1500000
1000000
500000
D
ratio of axonal growth compared to pre-injury
AJ
B6
CAST
NOD
PWD
WSB
NZO
129
Ctrl
ID8
E
no_drug, no_damage
id8, no_damage
no_drug, cut
id8, cut
Leading logFC dim 2
Leading logFC dim 1
F
cellular response to hypoxia
neuron projection
Enrichment
B6 no inhibitor cut
WSB no inhibitor cut
Statistic
G
Phenotype
abs(log2 fold changes)
Regulon
Olig2
Creb5
Ascl1
H
cell adhesion
central nervous system myelination
Enrichment
B6 Cut ID8
WSB Cut ID8
Statistic
I
Isoform switch in Ncoa4 (b6 no drug, cut vs wsb no drug, cut)
Gene Expression
Isoform Usage
Isoform Fraction (IF)
Condition
b6.no drug.cut
wsb.no drug.cut
ns
ENSMUST00000111994
ENSMUST00000163336
ENSMUST00000169722
J
B6
WSB
Pre
Post
axonal area (um2)
PRE
POST

FIGURE 10

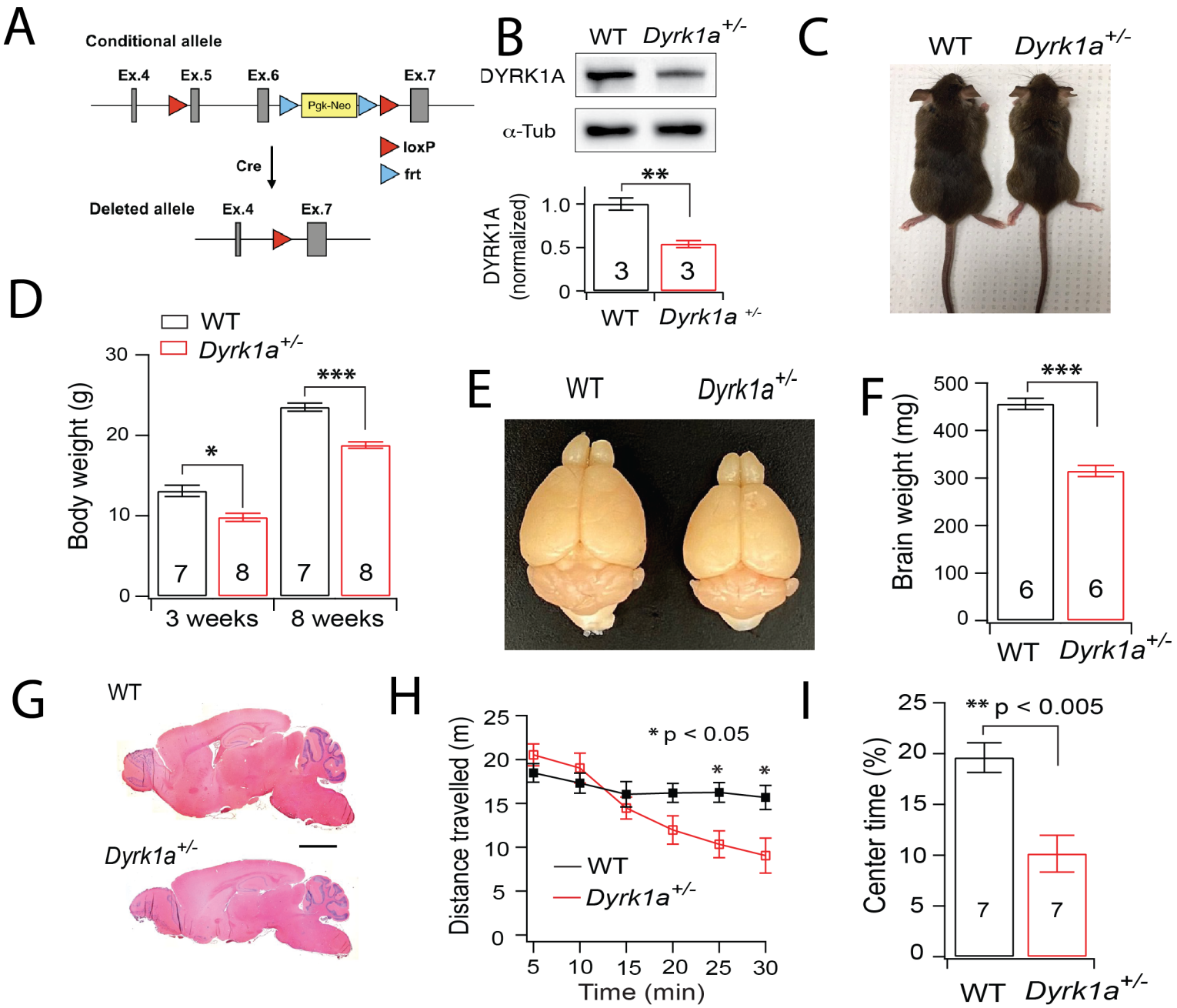
A
Conditional allele
Ex.4
Ex.5
Ex.6
Pgk-Neo
Ex.7
loxP
frt
Cre
Deleted allele
Ex.4
Ex.7
B
WT
Dyrk1a+/-
DYRK1A
α-Tub
DYRK1A (normalized)
1.0
0.5
0
**
3
3
WT
Dyrk1a +/-
C
WT
Dyrk1a+/-
D
WT
Dyrk1a+/-
Body weight (g)
30
20
10
0
*
***
7
8
7
8
3 weeks
8 weeks
E
WT
Dyrk1a+/-
F
Brain weight (mg)
500
400
300
200
100
0
***
6
6
WT
Dyrk1a+/-
G
WT
Dyrk1a+/-
H
Distance travelled (m)
25
20
15
10
5
0
* p < 0.05
*
*
WT
Dyrk1a+/-
5
10
15
20
25
30
Time (min)
I
Center time (%)
25
20
15
10
5
0
** p < 0.005
7
7
WT
Dyrk1a+/-